UNIVERSITY OF MINNESOTA

Three-Dimensional Simulation of Bridge Foundation Scour on Mississippi River Bridges 9321 & 27801

Final Report

Fotis Sotiropoulos

St. Anthony Falls Laboratory
University of Minnesota

CTS 16-03

CENTER FOR
TRANSPORTATION STUDIES

UNIVERSITY OF MINNESOTA

Technical Report Documentation Page

1. Report No.	2.	3. Recipients Accession No.	
CTS 16-03			
4. Title and Subtitle Three-Dimensional Simulation of Bridge Foundation Scour on Mississippi River Bridges 9321 & 27801		5. Report Date February 2016 6.	
7. Author(s) Fotis Sotiropoulos, Ali Khosronejad		8. Performing Organization Report No.	
9. Performing Organization Name and Address University of Minnesota St. Anthony Falls Laboratory 2 3rd Ave SE, Minneapolis, Minnesota 55414		10. Project/Task/Work Unit No. CTS #2015014 11. Contract (C) or Grant (G) No. (c) 99008 (wo) 160	
12. Sponsoring Organization Name and Address Center for Transportation Studies University of Minnesota 200 Transportation and Safety Building 511 Washington Ave. SE Minneapolis, MN 55455		13. Type of Report and Period Covered Final Report 14. Sponsoring Agency Code	
15. Supplementary Notes http://www.cts.umn.edu/Publications/ResearchReports/			

16. Abstract (Limit: 250 words)

We present data-driven numerical simulations of 100- and 500-year floods events in the Mississippi River at its intersection with the Highway I-694 by coupling coherent-structure resolving hydrodynamics with bed morphodynamics under live-bed conditions. The study area is about 1.7 miles long and 220 yard wide reach of the Upper Mississippi River, near Minneapolis MN, which contains several natural islands and man-made hydraulic structures. We employ the large-eddy simulation (LES) and bed-morphodynamic modules of the Virtual Flow Simulator (VFS-Rivers) model, a recently developed in-house code, to investigate the flow and bed evolution of the river along the reach and near the bridge piers BR 27801 and BR 932. We integrate data from airborne Light Detection and Ranging (LiDAR), sub-aqueous sonar apparatus on-board a boat and total station survey to construct a digital elevation model of the river bathymetry and surrounding flood plain, including islands and bridge piers. A field campaign under base-flow condition is also carried out to collect mean flow measurements via Acoustic Doppler Current Profiler (ADCP) to validate the hydrodynamic module of the VFS-Rivers model. Our simulation results for the bed evolution of the river under the 100- and 500-year flood reveal complex sediment transport dynamics near the bridge piers consisting of both scour and refilling events due to the continuous passage of sand dunes. A brief description of the findings in terms of maximum scour depth around individual bridge piers can be found in the executive summary of the report.

17. Document Analysis/Descriptors	18. Availability Statement		
Mississippi River, Rivers, Scour, Bridge Piers, Simulation, Floods, Silting, Streambeds	No restrictions. Document available from: National Technical Information Services, Alexandria, Virginia 22312		
19. Security Class (this report)	20. Security Class (this page)	21. No. of Pages	22. Price
Unclassified	Unclassified	58	

Three-Dimensional Simulation of Bridge Foundation Scour on Mississippi River Bridges 9321 & 27801

Final Report

Prepared by:
Fotis Sotiropoulos
Ali Khosronejad
St. Anthony Falls Laboratory
University of Minnesota

February 2016

Published by:
Center for Transportation Studies
University of Minnesota
200 Transportation and Safety Building
511 Washington Ave. SE
Minneapolis, MN 55455

Table of Contents

List of Figures

List of Tables

Executive summary

We carried out a coupled flow and sediment transport simulation of the Mississippi River at its intersection with Interstate I-694 under 100-year flood conditions. The simulation results showed that the bridge piers 2, 3, and 4 of BR 27801 downstream Pier and piers 3 and 4 of BR 9321 Center Pier will experience significant scour depths. The summary of the simulation results of the 100-year flood for these piers is as follows:

- Pier 2 of BR 27801 downstream Pier experiences a maximum scour depth of 30 ft. Given the current level of bed elevation at the pier (~790 ft.), the scour depth of 30 ft. leads to ~5 ft. exposure of its pile.
- Piers 3 and 4 of BR 27801 downstream Pier experience maximum scour depths of 18 ft. and 25 ft., respectively. Given the current bed elevations at these piers that are ~795 ft. and ~798 ft., respectively, none of the two pier's piles will be exposed. The scour depth at these two piers reaches the top of their pile system.
- For pier 3 of BR 9321 Center Pier the simulated maximum scour depth is 27 ft. and its current bed elevation is ~795 ft. This scour depth exposes 21 ft. of its pile system at which point the pier system has ~15 ft. of its length to bear the load.
- For pier 4 of BR 9321 Center Pier the simulated maximum scour depth is 6 ft. and its current bed elevation is at ~797 ft. The maximum scour depth reaches to the top of its pile system, without exposure of the piles.

The coupled flow and sediment transport simulation of the 500-year flood event in the Mississippi River at its intersection with Interstate I-694 was also carried out. According to the simulation results for this case, the bridge piers 2, 3, and 4 of BR 27801 downstream Pier and piers 2, 3, and 4 of BR 9321 Center Pier experience significant scour depths. The summary of the simulation results of the 500-year flood for these piers is as follows:

- Pier 2 of BR 27801 downstream Pier experiences a maximum scour depth of 28.1 ft. Given the current level of bed elevation at this pier (~790 ft.), the scour depth of 28.1 ft. leads to ~3 ft. exposure of its pile.
- Piers 3 and 4 of BR 27801 downstream Pier will experience maximum scour depths of 26 ft. and 28.3 ft., respectively. Given the current bed elevations of these piers that are at ~795 ft. and ~798 ft., respectively, pier 3 of BR 27801 downstream Pier will have ~1 ft. of its pile system exposed, while pier 4 of BR 27801 downstream Pier will experience no pile exposure. The maximum scour depth of pier 4 of BR 27801 downstream Pier will, however, reach to the top of the pile system.
- For pier 3 of BR 9321 Center Pier the simulated maximum scour depth is 26.2 ft. and its bed elevation is currently at ~795 ft. This scour depth will expose ~20 ft. of its pile system and the pier will have ~15 ft. of its length to bear the load.
- For piers 2 and 4 of BR 9321 Center Pier the simulated maximum scour depths are 6.2 ft. and 5.1 ft., respectively, and given their current bed elevation the maximum scour depth will reach to the top of their pile systems, without exposure of the pile.

1. Introduction

Extreme river flooding events can lead to enormous economic losses and societal disasters. There are numerous hydrological-based forecasting tools that enable governments and local authorities to estimate the timing and magnitude of flood events. Such information can be used to set up an efficient flood alarm system to enhance the public safety, avoid human losses, and mitigate social damages (see for details Merkuryeva et al. 2015). It is also important to be able to assess the risk flooding poses on infrastructure stability. Such predictions require the use of hydraulic engineering numerical models, which are the focus of the present work.

For decades, computational fluid dynamics (CFD) has been utilized as an effective hydraulic engineering tool to study flow and sediment transport processes in rivers and streams under base-flow conditions (see, e.g., Olsen and Kjellesvig 1998, Nagata et al. 2005, Baranya et al. 2013). For rivers under flood conditions, however, the interaction among the turbulent flow, river bathymetry, hydraulic structures, and migrating bed forms becomes more challenging to simulate. Therefore, most of the existing numerical studies of river flooding in field-scale rivers utilize two-dimensional (2D) models, which solve the so-called shallow-water equations to predict the flood flow. Despite their many successful applications and wide-spread use in the hydraulic engineering practice, 2D models are inherently unable to simulate the dynamics of three-dimensional (3D) high-energy coherent flow structures and their effect on sediment transport and scour processes near complex hydraulic structures. Yet, such predictive capabilities are critically important for accurately assessing the risk extreme flooding on hydraulic structures.

Recent advances in computational algorithms and increasingly growing computing power have set the stage for developing powerful simulation-based tools for tackling such intricate hydraulic engineering problems. In this work we leverage recent computational advances to perform data-driven, coherent-structure resolving simulations of turbulence and morphodynamics during extreme flooding events for field-scale rivers.

The objective of this research is to predict the scour depths adjacent to each bridge pier of the Interstate 694 (Bridge No. 9321 and 27801) in the Mississippi River. To do so, we employ a comprehensive and quantitative numerical model of flow and sediment transport. The simulation domain includes approximately 1.2 miles of the river upstream of the bridge, all of bridge piers, and 0.5 mile of the river downstream of the bridge. The first phase of the project consisted of collection of bathymetry and flow field data that was carried out by Minnesota Department of Transportation (MnDOT) personnel and successfully transferred to the research team at St. Anthony Falls Lab (SAFL) of the University of Minnesota. The important part of the data transfer from the MnDOT to the SAFL was to ensure that the MnDOT's sonar data for river bed bathymetry and Acoustic Doppler Current Profiler (ADCP) data correctly line up with the existing LiDAR data for the study area. This alignment is important because we combined the sonar (i.e. the river bed bathymetry below water surface) and LiDAR (i.e. the river bathymetry above water surface) data to construct the complete geometry of the river in the study area.

In order to validate the flow field computations of the model, the large-eddy simulations (LES) results of the flow field under base-flow conditions have been compared with corresponding ADCP flow data collected by the MnDOT personnel. The LES results of the base-flow at the region immediately upstream of the bridge show that the near-bed flow velocity near to the right (west) bank of the river is significantly higher than that of the left (east) bank. Farther upstream, however, the simulated velocity distribution in the two tributaries of the Island of Peace switch sides so that the near-bed velocity in the west tribute is lower than that of the

east tribute. The simulated velocity distributions correspond with the MnDOT bed bathymetry measurements. More specifically, the MnDOT measured bathymetry shows deeply scoured regions at places where the LES model yields high near-bed velocities. For more details on this issue the reader is referred to the quarterly report for period March 15, 2015 to June 15, 2015 in Appendix I to this report.

The main focus of the rest of this report is on the coupled flow and bed morphodynamics simulation of 100- and 500-year flood events within the study area to quantitatively predict the maximum scour depth adjacent to each bridge pier of Bridge No. 9321 of the I-694 freeway. The coupled flow and bed morphodynamics simulations, for the 100- and 500-year floods, are carried out in two different scales: (1) far-field modeling, which includes the entire study reach (1.7 mile) and (2) near-field, high resolution, modeling of the region adjacent to the bridge piers. By carrying out the simulations in two scales we effectively reduced the computational costs of the study, while we maintained the resolution of the simulations at an appropriate level.

2. Geometric data of the study area

We acquired the bathymetry data of the river bed, river banks, and bridge piers from three different sources: (1) sub-aqueous sonar installed on-board of a boat; (2) airborne LiDAR; and (3) traditional surveying methods, respectively. We used a combination of airborne LiDAR, sub-aqueous sonar, and hydrometry station data to reconstruct the water surface elevation of the river for various flow and flood conditions.

The airborne LiDAR data was used to construct the river bathymetry above the normal water surface. In Figure 1(A) we illustrate the river bathymetry above the water surface obtained from LiDAR data. To acquire the river bathymetry below water surface, the MnDOT carried out a field campaign measuring the bed bathymetry of the river using a sub-aqueous sonar apparatus installed on-board a boat. Like LiDAR data, the sonar data was collected during the base-flow condition. The plot in Figure 1(B) is the combination of the LiDAR and sub-aqueous sonar data. The two data-sets construct a complete bathymetry data set for the study area.

Water surface elevation for the 100- and 500-year flood events were constructed by applying the corresponding depth information (Toso, 1993) to the measured base-flow water surface elevation. To do so, we raised the measured-water-surface-elevation of the base-flow in vertical direction. Figure 1(C) is the combination of the LiDAR data and the constructed water surface for the 100-year flood.

Finally, in a separate field campaign, a surveying team used a total station to survey the geometry of the bridge piers. The geometry of each individual pier was transferred into the river bed bathymetry data (see Figure 1(D)-(E)). The completed geometry of the study area with bride piers was then meshed and used in the numerical simulations (Figure 1(F)).

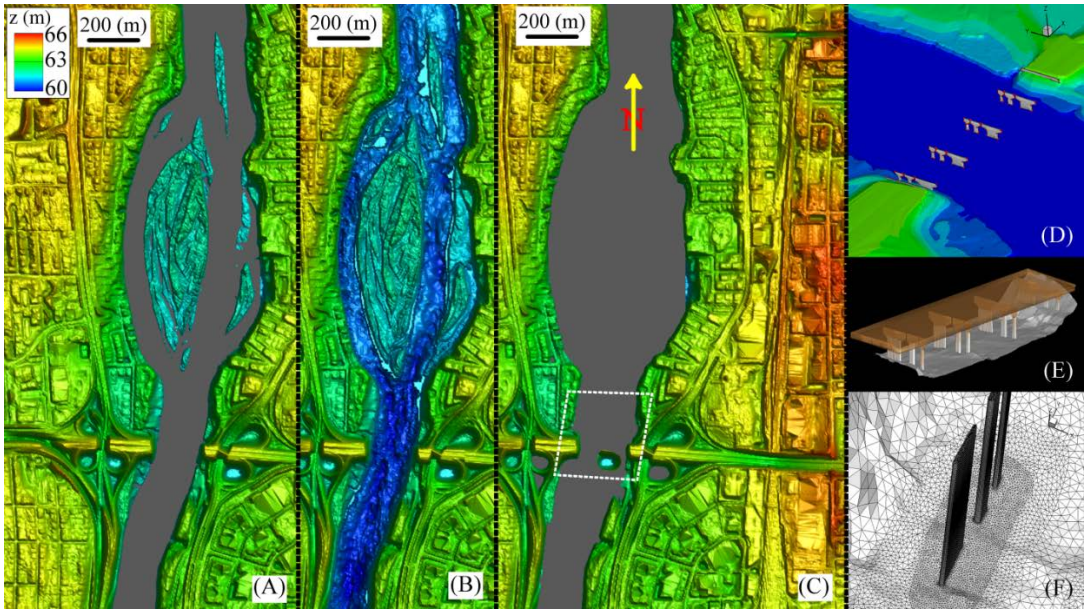

Figure 1: Geometrical data of the study area: (A) LiDAR data for river bathymetry above water surface under base-flow condition; (B) combination of LiDAR data for river bathymetry above water surface and sub-aqueous sonar measurements for river bed bathymetry to obtain the complete bathymetry of the river; (C) combination of LiDAR data for river bathymetry above water surface and hydrologic data of Toso (1993) to obtain the water surface of 100-year flood; (D) laser scanned data for the geometry and location of bridge piers; (E) positioning of the bridge piers and top slab in the river; (F) unstructured meshing of the river bed bathymetry and bridge piers. Elevations are above an arbitrary datum. Dashed-white line in (B) shows the region where near-field simulation for 100-year flood event is carried out. Flow in (A)-(C) is from top to bottom.

3. River flow characteristics

We summarize in Table 1 the flow characteristics of the Upper Mississippi river within the study area. The flow field data for the base-flow condition is obtained from the MnDOT field campaign in which they used ADCP and sub-aqueous sonar to measure the flow velocity and water depth, respectively. The discharge of the river for the base-flow, during the field campaign, was measured (via ADCP) to be 283.0 m^3s^{-1}. This base-flow discharge is verified by United States Geological Survey (USGS) measurement station near the study site, which reported a discharge of 283.2 m^3s^{-1} for the same day.

Table 1: Characteristics of flow field for the study area in the Upper Mississippi River with Q, H, and Ub being the flow discharge, the mean flow depth, and the bulk velocity, respectively (Toso, 1993).

Flow condition	Q (m^3s^{-1})	H (m)	$U_b(ms^{-1})$
Base-flow	283.0	4.0	1.38
100-year flood	2780.2	8.0	1.87
500-year flood	3667.0	9.2	2.08

4. Model validation

The coupled flow and bed morphodynamics computations of the model have been extensively validated for micro- to macro-scale open channels under live and clear-water scour conditions. For details of these morphodynamics validations the reader is referred to Kang et al. 2011; Kang and Sotiropolous 2011; and Khosronejad et al. (2011; 2012; 2013; 2014a,b; 2015). A complete version of this flow field validation study is already reported in the quarterly report for the period of January 14, 2015 to March 15, 2015, which can be also found in Appendix II of this report. In this section we present a summary of the flow field validation study using the MnDOT's ADCP measurements along four cross sections shown in Figure 2. Due to the movement of the boat, the ADCP measurements are carried out along the four irregular paths shown in Figure 2 (A). The measured data along these irregular paths are projected to the four straight lines shown in Figure 2(B) where we compared them with the simulation results. In order to project the ADCP data onto the four straight lines we employed a velocity mapping software, which is developed by U. S. Geographical Survey (USGS) and can be found online at *https://hydroacoustics.usgs.gov/movingboat/VMT/VMT.shtml*.

In Figure 3 the measured velocity magnitude (from ADCP measurements) is compared with LES along the four cross-sections shown in Figure 2(B). The ADCP data in Figure 3 are instantaneous values while the LES results are time-averaged over flow-through time (i.e. the time it takes for water particles to enter and exit the domain, which for the base-flow is ~15min). Because of the complexity of the river flow and movements of the boat on which the ADCP is mounted, the depth-averaged measured data show a significant fluctuation. However, the LES captured results agree reasonably well with the measurements and the peaks in velocity magnitude at different cross-sections.

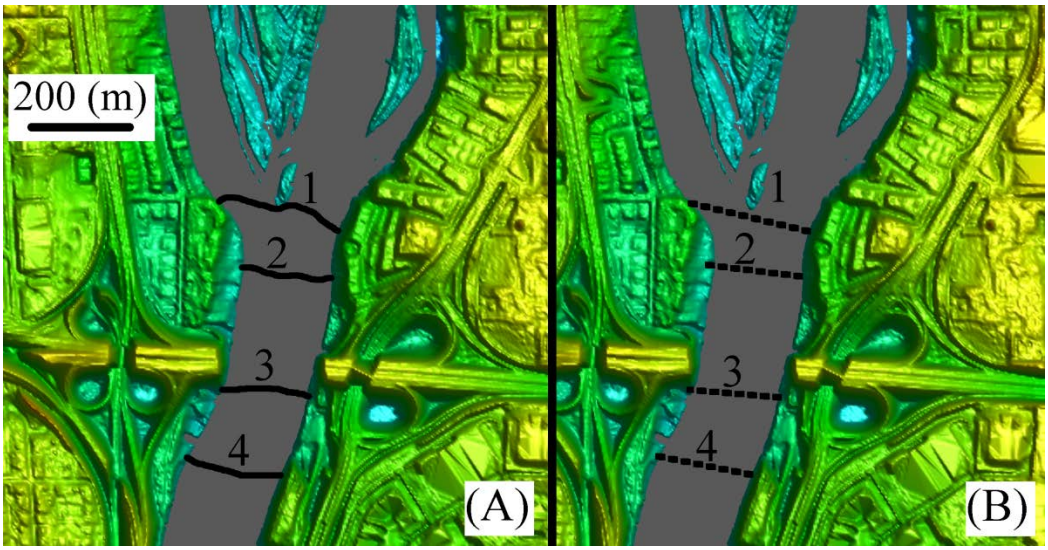

Figure 2: Location and paths of the ADCP flow field measurements under base-flow conditions: (A) along irregular paths of the boat (original ADCP) and (B) after projection onto the straight lines using the velocity mapping software of USGS, which is designed to project the velocity components along an irregular path onto straight lines. The velocity mapping software can be found at https://hydroacoustics.usgs.gov/movingboat/VMT/VMT.shtml. Flow is from bottom to top.

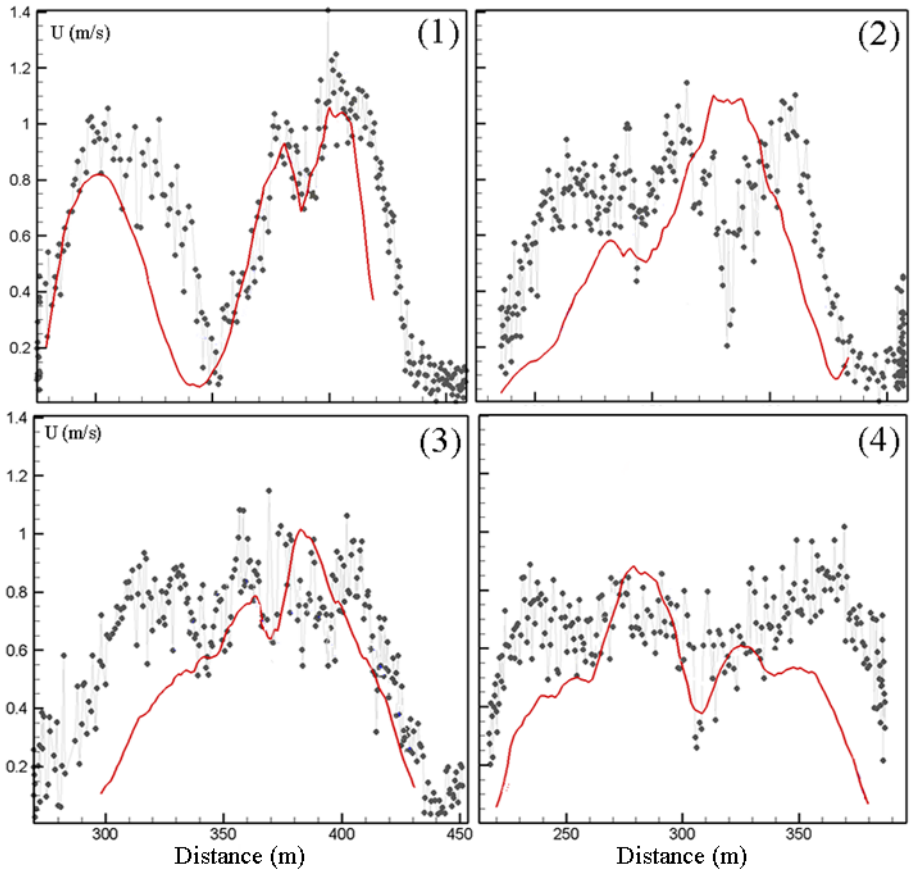

Figure 3: Comparing the depth-averaged velocity magnitude of ADCP measurements (gray dots) with the depth- and time-averaged LES results (red lines) along the width of the river (S) in cross sections (1) to (4) illustrated in Figure 2(B). Discrepancies between the simulation and measured data are mainly due to the uncertainty in the field data and the fact that these data are instantaneous while the LES results are time-averaged. The time scale of the flow structures in the river downstream of the island have a time scale of about 30 min and given the instantaneous nature of the measured data such fluctuations and consequently discrepancies are expected.

5. Coupled flow and morphodynamics simulation of 100-year flood

5.1. Far-field simulation

In order to simulate the far-field domain we employed a background grid system with over 94 million computational grid nodes and the river bed was meshed with over 140,000 unstructured triangular cells. The spatial resolution of the far-field simulation is ~0.2m. The temporal resolutions for the flow and bed morphodynamics calculations are 0.2 sec and 30 sec, respectively. The disparity in these two time steps is in accordance with the dual time-stepping technique developed by Khosronejad et al. (2014a). We first simulated the flow field for the 100-year flood (without sediment transport module activated) to produce a fully developed turbulent flow and suspended sediment load distribution in the entire study reach. Once the fully turbulent flow is developed we stopped the calculation and saved the flow and suspended sediment concentration field as the initial boundary condition of the 100-year flood condition (for more details of the 100-year flood characteristics see the quarterly report of the period March 15, 2015 to June 15, 2015 in Appendix I).

The coupled flow and morphodynamics simulation is then started and continued until the bed morphology reached quasi-equilibrium, which is when the bed change over a flow-time (i.e. the time it takes for the fluid particle to travel from the inlet to the outlet of the study reach) is less than five percent. We plot in Figure 4 the snapshots of simulated flow field at the free-surface. Development of scour geometry around bridge piers at t=5 days rendered highly complex bed geometry, which in turn modified the flow field downstream of the bridge. The deformation of mobile bed throughout the study reach can be seen in Figure 5, where we plot the contours of bed elevation for the same instants in time. Dynamic evolution of the river bed and turbulent flow in the far field domain can also be seen in the two video clips on the YouTube at *https://youtu.be/rcVTdeT82z4* and *https://youtu.be/z6xN7rojYoM*.

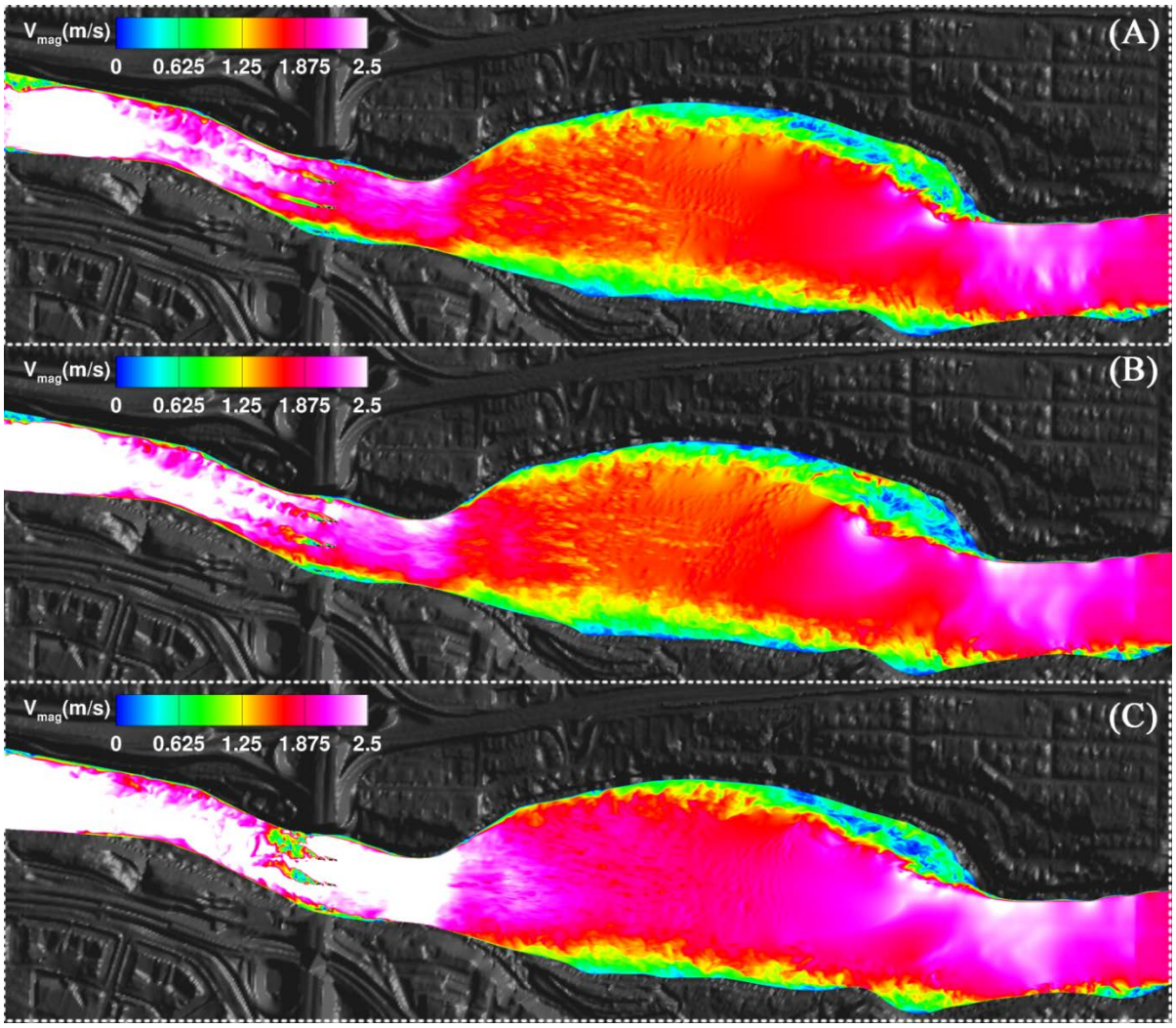

Figure 4: Snapshots of simulated flow field (velocity magnitude) at the water-surface over a deforming bed morphology (coupled simulations) after (A) t=0, (B) t=2.5 days, and (C) t=5 days. Flow is from right to left. Note that at t=5 days the scour hole geometry becomes significantly complex and deep. Such complexity is evident from the turbulent structures that are shed from the scour hole geometry and reach free-surface in (C).

The development of scour pattern in the far-field simulations is largely due to the large-scale sediment transport processes through the river. This process is driven by the highly turbulent and high-energy coherent flow structures of the 100-year flood flow. The interaction of the mobile bed and flow field can be seen in Figure 6, where we show the contours of velocity magnitude over a translucent free-surface with the evolving mobile bed below it. The sediment material (i.e. mostly bed material with some suspended material) is transported from upstream regions of the river toward the bridge and travels though the spanswise and streamwise gaps between the bridge piers. This migration occurs in the form of large-scale dunes and gives rise to fluctuating scour depths near individual bridge piers.

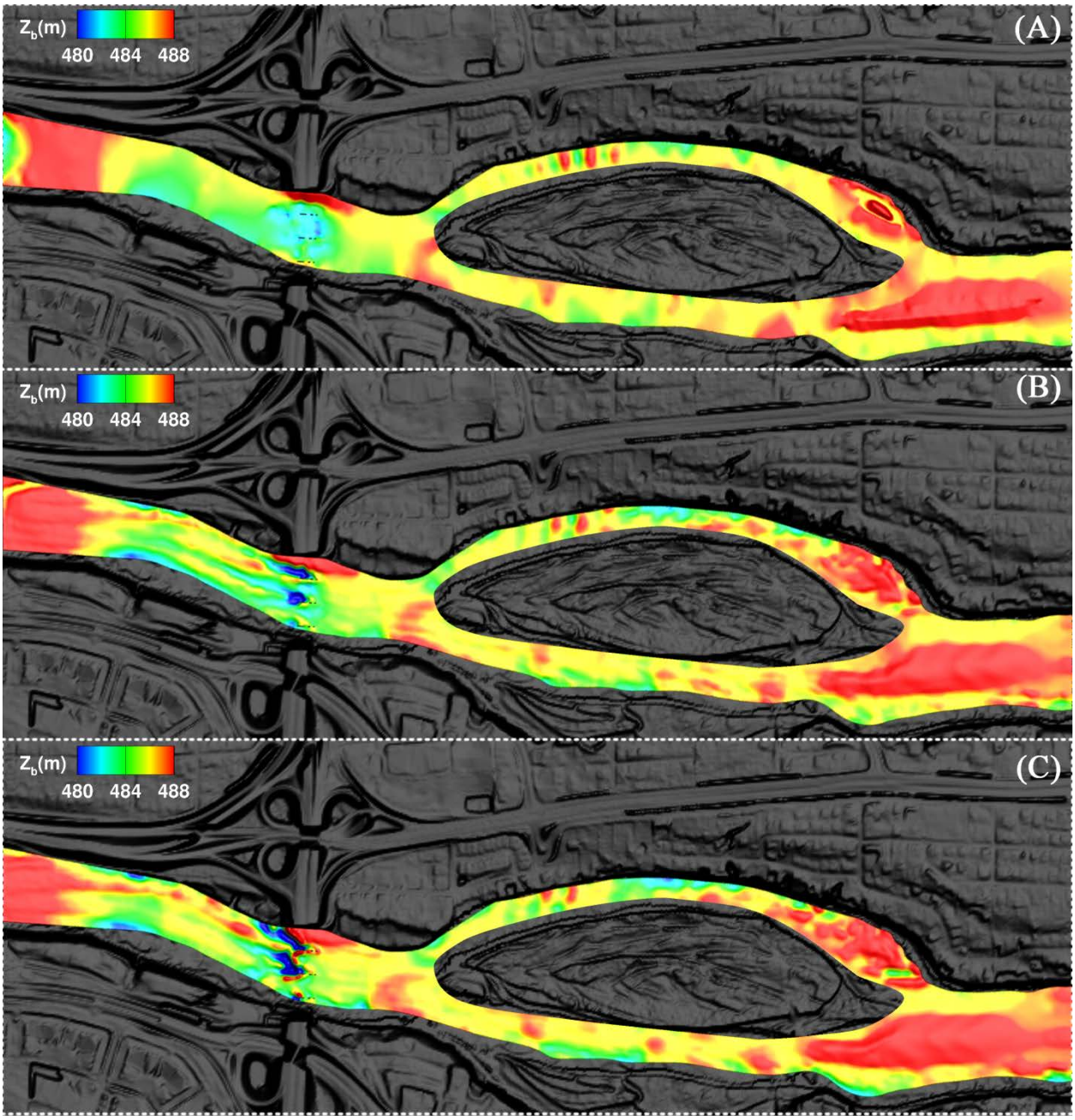

Figure 5: Snapshots of simulated bed elevations after (A) t=0, (B) t=2.5 days, and (C) t=5 days. Flow is from right to left. Note that the island upstream of the bridge is assumed to be immobile.

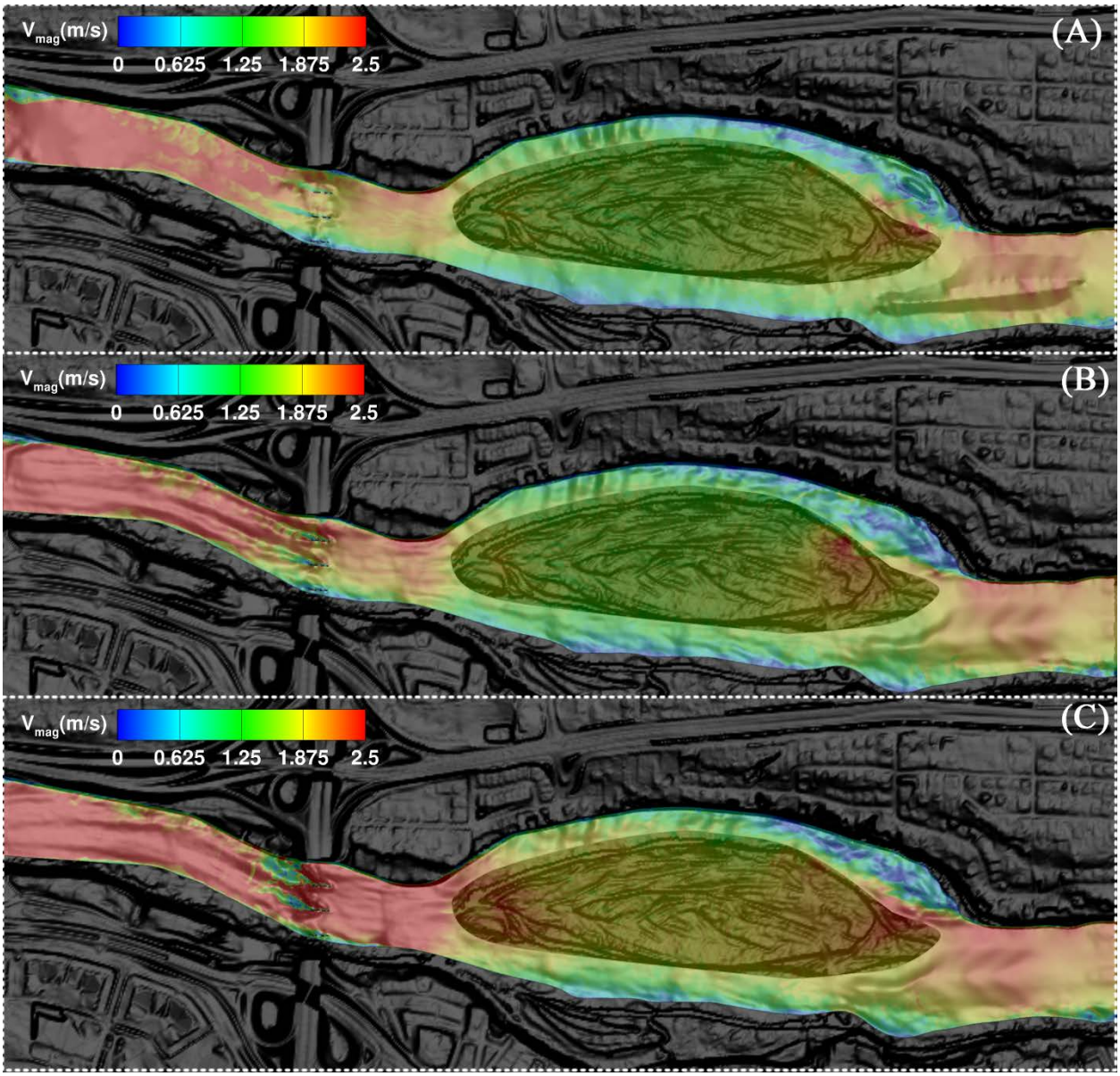

Figure 6: Snapshots of simulated flow field (velocity magnitude at free-surface) over the bed morphology after (A) t=0, (B) t=2.5 days, and (C) t=5 days. Flow is from right to left. Note that the free-surface is rendered translucent so that the bed morphology below it becomes visible.

To analyze the structural susceptibility of each bridge pier to such large-scale sediment transport processes, we continued the 100-year flood event for more than 20 days. Since such a flood is very unlikely to last more than 20 days we report only 20 days of data in here. During the course of the simulations we saved the hydro- and bed-morphodynamics simulation results. We extracted time series data of the scour depth adjacent to each bridge pier. Each individual bridge pier is denoted using the array shown in Figure 7 in which R, M, and L stands for right, middle, and left piers. For each bridge pier we collect and examine the time series of bed elevation at several points around the pier. Subsequently, for each pier we select a representative local point at which the maximum scour depth is experienced. The time series of the bed elevation at so-obtained local points around each bridge pier are shown in Figure 8.

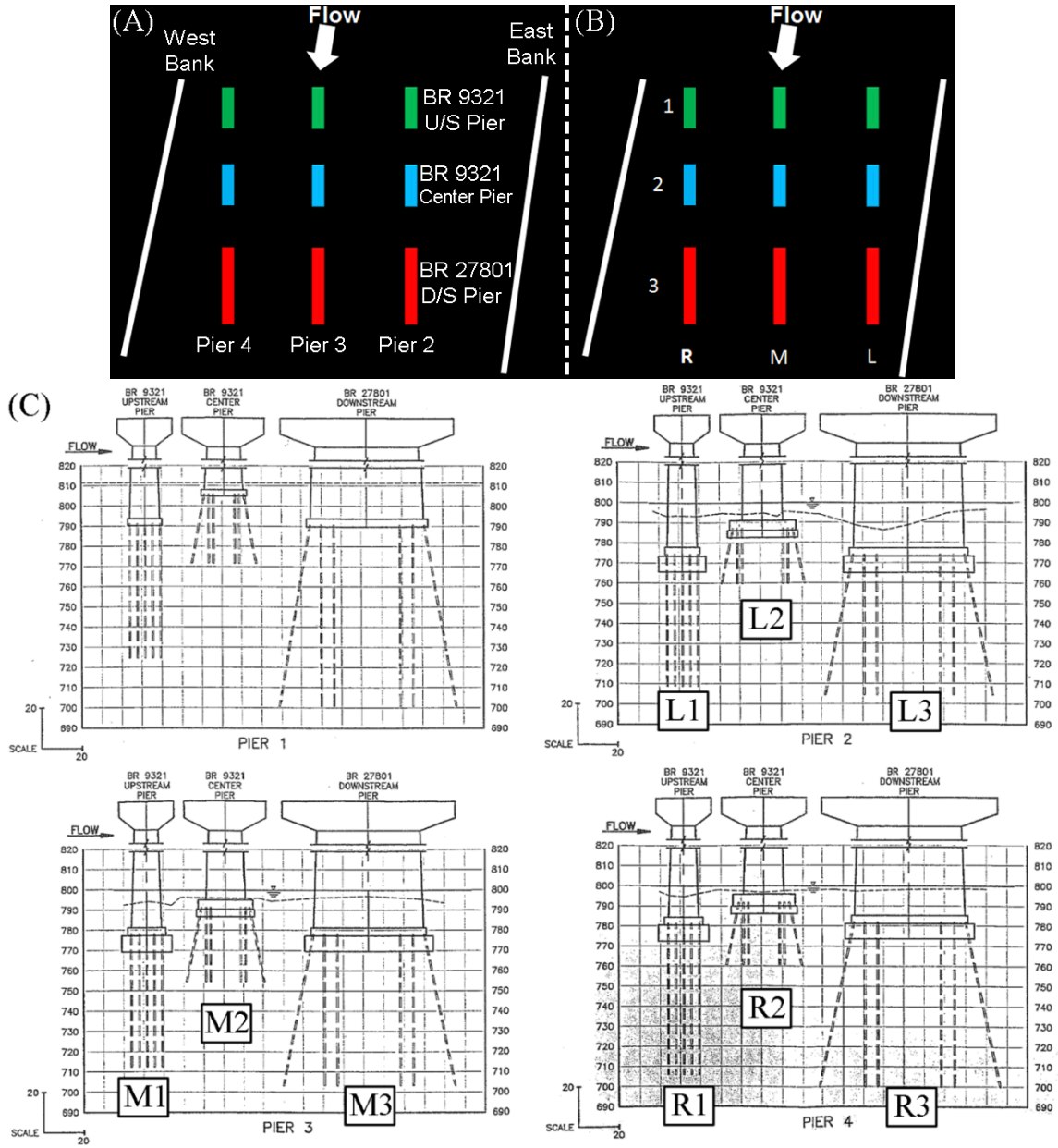

Figure 7: Schematic of bridge piers and their naming: (A) MnDOT standard names; (B) names used in this report; and (C) MnDOT's sketch of bridge piers. The names shown in (A) are based on the naming used in MnDOT documentations (Toso, 1993) in which U/S and D/S stand for upstream and downstream, respectively. We in (B) develop a new naming to facilitate the reporting process. The new naming in (B) can be easily associated to the standard naming. The piers on the right bank, left bank, and middle are named R, L, and M, respectively, while from upstream to downstream they are number from 1 to 3. R, M, and L in (B) are Pier 4, Pier 3, and Pier 2 in (A). 1, 2, and 3 in (B) are BR 9321 U/S Pier, BR 9321 Center Pier, and BR 27801 D/S Pier in (A), respectively. White lines on the side are the river banks. Flow is from top to bottom. Note that Pier 1 is not included in the flood flow simulations.

In Figure 8 we plot the time series of scour depth at the local points (with the maximum scour depth) around each bridge pier. As shown in this figure, the three bridge piers at the most downstream locations (L3, M3, and R3) experience the maximum scour depth. We note that footprint of the large scale dunes passing through the bridge can be seen in the large scale

fluctuations in these time series of scour depth. Negative values in these time series mean that at some points in time the selected local point have experienced deposition.

Based on these simulated time series in Figure 8, one can readily see that the bridge pier R3 experiences a total of ~20 feet scour depth at least on part of its base, while L3 and M3 will experience slightly milder scour depths of ~15 ft. and ~8 ft. However, we also note that for such deep scour holes to develop, the 100-year flood is required to last for 20 days (see Figure 8). In Table 2 we present a summary of the maximum scour depth during the 100-year flood at a local point around each bridge pier along with the duration of time that the maximum scour depth persists.

Table 2: Summary of simulated maximum scour depth near each bridge pier (see also Figure 7 for bridge pier identity) under 100-year flood event in the far-field simulation. D_{sf} is the maximum scour depth at a local point around the pier, third column is the location of the local point around the pier, and the fourth column is the maximum time during which the pier experiences the maximum scour depth at the local point. The fourth column, the duration of scour depth, is based on the assumption that the 100-year flood continues for 20 days.

Pier	D_{sf} (ft.)	Location	Duration
L1	2	West side	~ 1 day
L2	4.8	West side	~ 0.5 day
L3	15	East side	~ 10 days
M1	1	Near downstream end	~ 0.2 day
M2	2	East side	~ 2 days
M3	8	West side and near downstream end	~ 2 days
R1	0.5	Near downstream end	0.1 day
R2	5	West side and near downstream end	~ 2 days
R3	20	West side and near downstream end	~10 days

5.2. Transition from far-field to near-field

In order to simulate the coupled flow and bed evolution at the region near the bridge piers with a higher resolution than that of far-field simulations, we carried out another simulation for a much smaller region in the middle of the larger study reach. The near-field region in this study is limited to ~0.12 mile upstream and ~0.08 mile downstream of the bridge location (see Figure 9). We used a background grid with 34.4 million computational nodes along with ~50,000 unstructured triangular elements for the river bed. The spatial resolution for the coupled hydro-morphodynamics is ~0.1 m and the temporal resolutions for hydro- and morpho-dynamics are 0.15 sec and 25 sec, respectively.

In order to take into account the complex flow pattern at the confluence of the two branches at the upstream location on the transport processes in the near-field region, we carried out a separate flow field only simulation and saved the flow field at the near-field's inlet cross-section (see Figure 10). This cross-sectional velocity field then was interpolated into a finer grid resolution at the inlet of the near-field region (Figure 11) and was used as the inlet boundary condition for the flow field of the near-field simulations.

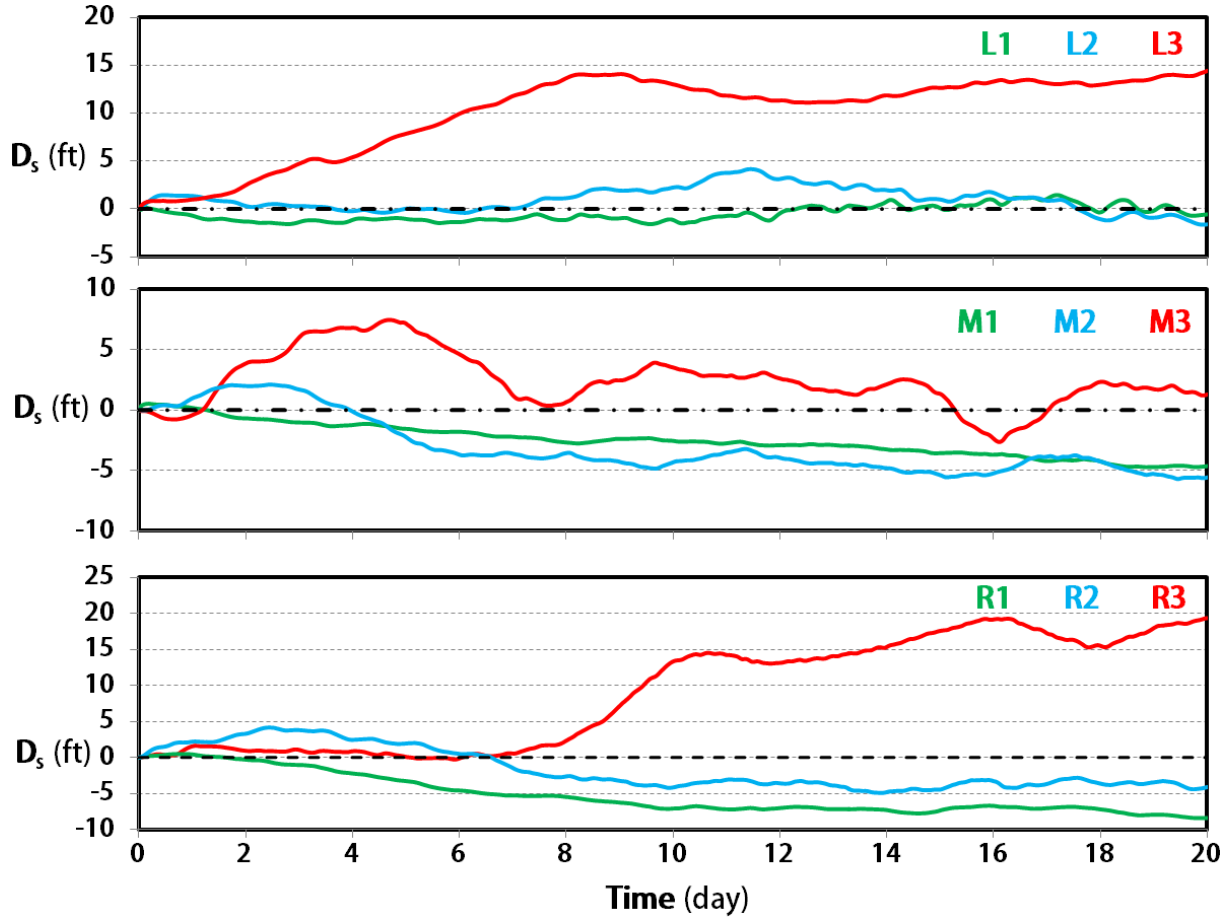

Figure 8: Far-field simulated time series of scour depth (Dsf) around individual bridge pier at the local point with the maximum scour depth for the 100 flood event.

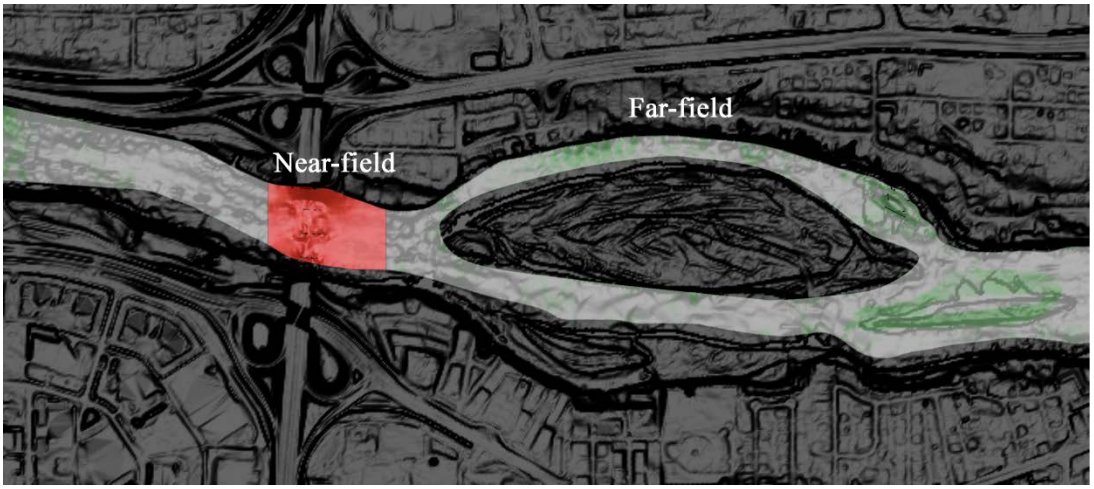

Figure 9: Far-field (the entire reach) and near-field (the red-colored reach) regions in the simulations. Flow is from right to left.

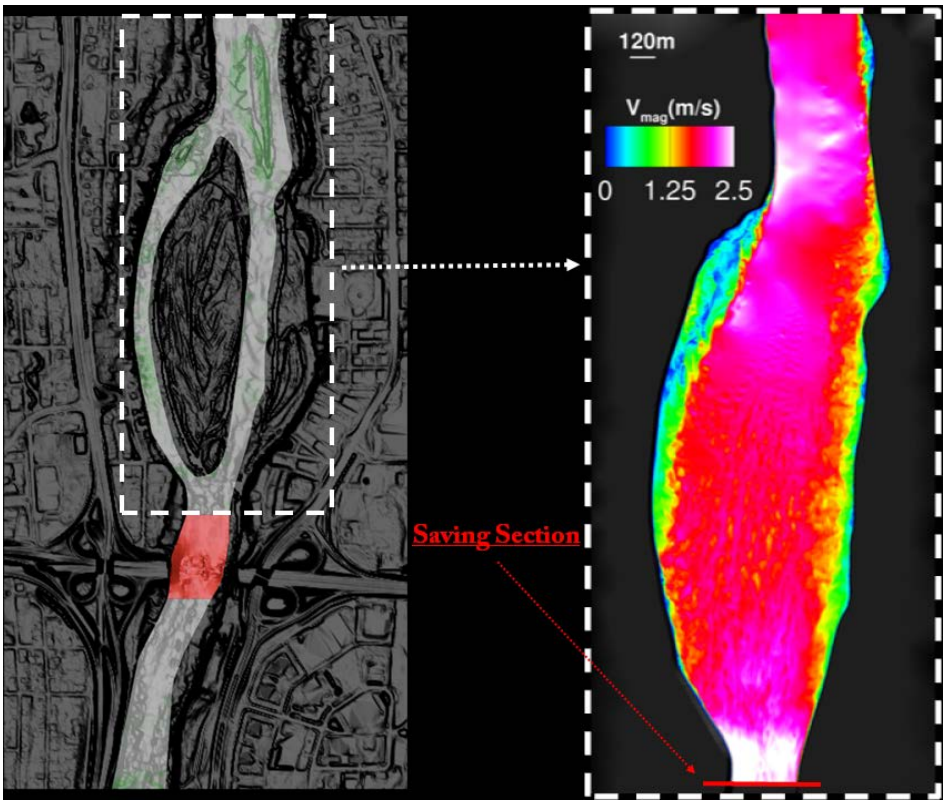

Figure 10: The simulation domain used to develop inlet boundary condition for the near-field region to take into account the effect of the confluence on the flow field of the near-field simulation. Flow field is saved at the last cross-sectional area (red-line). Flow is from top to bottom.

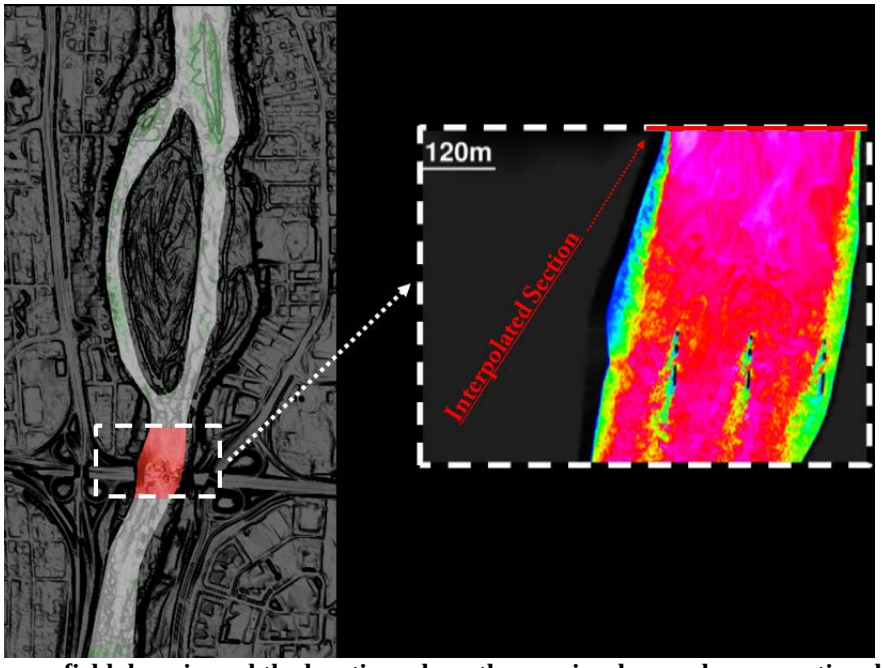

Figure 11: The near-field domain and the location where the previously saved cross-sectional flow is applied as the inlet boundary condition for the flow field. Flow is from top to bottom.

5.3. Near-field simulation

We first developed a fully turbulent flow over the entire near-field region and used it as an initial condition for the flow field. Then the coupled hydro-morphodynamics simulation started (during which the previously saved cross-sectional velocity field was used as the inlet boundary condition) and continued for ~15 days until the mobile bed reached quasi-equilibrium. At each time step, the total sediment mass exiting the near-field domain at its outlet section is calculated as the total sediment out-flux. In the next time step, the so-computed sediment out-flux is fed at the inlet of the near-field as the inlet boundary condition. In Figure 12 we show snapshots of the near-field simulation at one instant; where one can readily see the complex interaction of turbulent flow, scour hole and bridge piers.

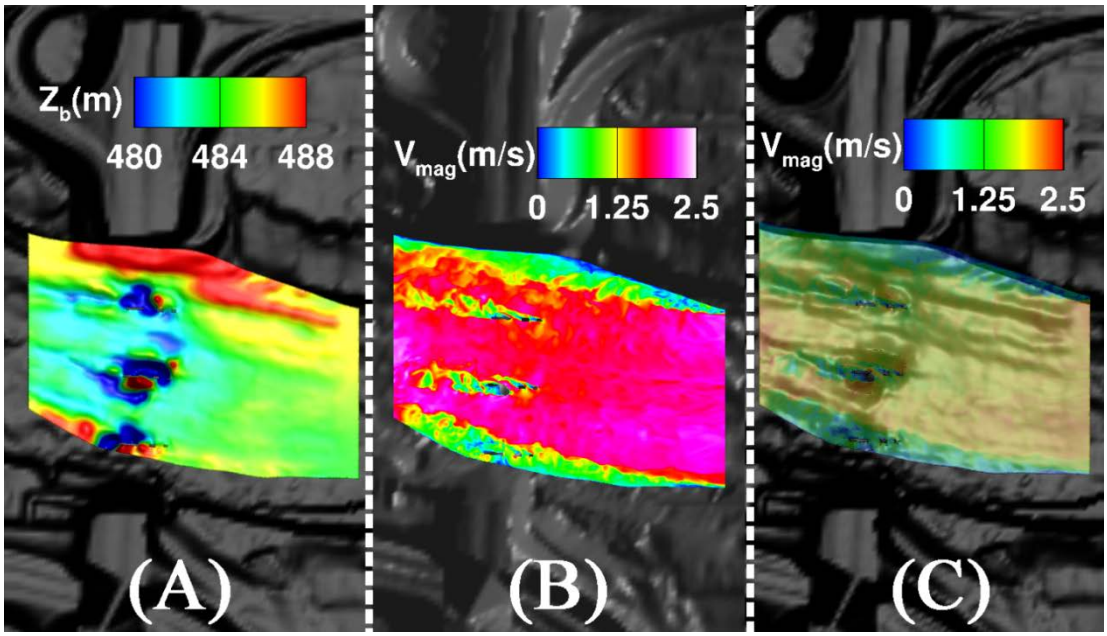

Figure 12: Snapshots of simulated coupled hydro-mophodynamics at t =5days for: (A) contours of bed elevation; (B) flow field (velocity magnitude) at the water-surface; and (C) flow field (velocity magnitude) at the water-surface over a deforming bed morphology. Flow is from right to left.

The near-field simulation has a higher resolution, and therefore we expect to resolve more of the high-energy eddies that are responsible for local scour around individual bridge piers. Since the migration of large-scale dune waves along the river is not simulated in the near field, their foot prints on the developing scour hole geometry is absent. However, it's important to employ the near-field coupled simulation to predict the effect of dynamically rich and high-energy coherent structures on the development of scour geometry. The time series of scour depth development around individual bridge piers (see Figure 7 for the naming of each individual pier) from near-field simulation is shown in Figure 13. The scour depths in this figure should be taken into account in addition to those of the far-field simulation to make sure that both the effect of large-scale and local sediment transport is considered. In a conservative manner, one may consider the linear combination (addition or superposition) of the far- and near-field scour depth to be the total expected scour depth.

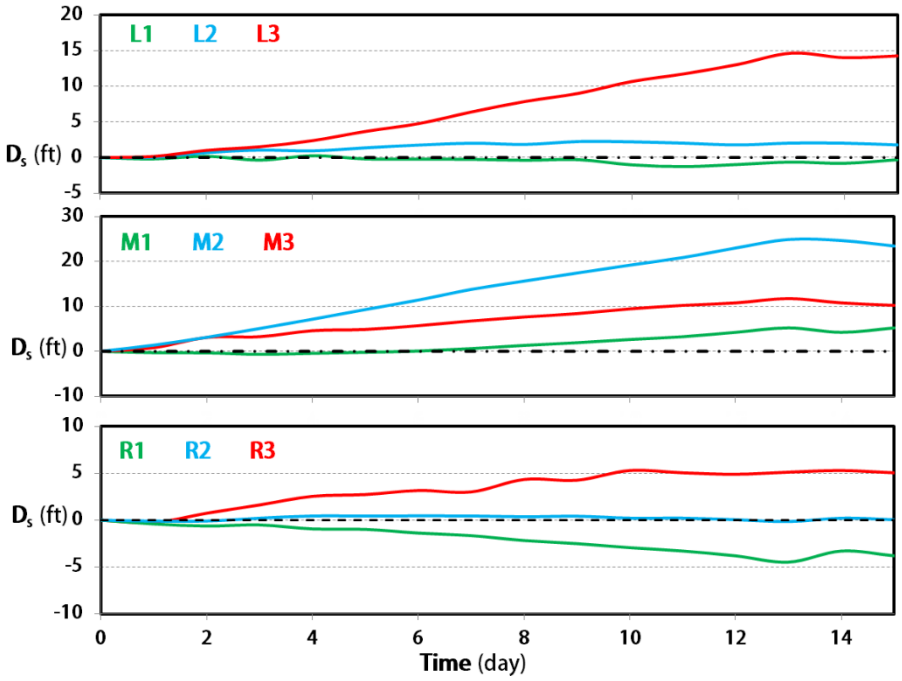

Figure 13: Near-field simulated time series of scour depth (D_{sn}) around individual bridge pier at the local point with the maximum scour depth for the 100 flood event.

On the basis of the near-field time series of scour depths; L3, M3, and R3 piers experience maximum scour depths of about 15 ft., 10 ft., and 5 ft., respectively. In Table 3 we show a summary of the simulated maximum scour depth for each bridge pier in the near-field simulation. Like the far-field case, the maximum scour depths in Table 3 are obtained by probing the time series of scour depth at various points around each pier and selecting the one that experiences the maximum scour.

Table 3: Summary of simulated maximum scour depth near each bridge pier (see also Figure 7 for bridge pier identity) under 100-year flood event in the near-field simulation. D_{sn} is the maximum scour depth at a local point around the pier, third column is the location of the local point around the pier, and the fourth column is the maximum time during which the pier experiences the maximum scour depth at the local point. The fourth column, the duration of scour depth, is based on the assumption that the 100-year flood continues for 15 days.

Pier	D_{sn} (ft.)	Location	Duration
L1	0.2	All around the pier	~ 1 day
L2	2.2	Front and West sides	~ 10 days
L3	15	West side and near downstream end	~ 3 days
M1	6	All around the pier	~ 3 day
M2	25	All around the pier	~ 3 days
M3	10	All around the pier	~ 5 days
R1	0.1	Near downstream end	~ 0.1 day
~R2	1	All around the pier	~ 5 days
R3	5	All around the pier	~7 days

In the far-field simulation, however, these three piers experienced maximum scour depths of about 15 ft., 8 ft., and 20 ft., respectively. Thus, it's safe to interpret that in the event of a 100-year flood the L3, M3, and R3 bridge piers will (at the local point around them) experience an overall maximum scour depth of about 30 ft., 18 ft., and 25 ft., respectively.

For other bridge piers for which time series show both deposition and scour, due to the passage of dunes or local effects in the far- and near-field simulations, respectively, it's safe to assume that the maximum scour depth they experience is the value of the maximum scour depth.

5.4. Maximum scour depth under 100-year flood condition

Details of the maximum scour depth for each individual bridge pier for the 100-year flood are shown in Table 4, where we summarize the simulations results of the far- and the near-field. The total maximum scour depths in Table 4 are calculated by simply summing the maximum scour depths from far- and near-field simulations.

Table 4: Summary of simulation results for maximum scour depth (in ft.) near each individual bridge pier (see also Figure 7 for bridge pier identity) under 100-year flood event. D_{st}, D_{sf}, and D_{sn} are the maximum total, far-field, and near-field scour depths (in ft.), respectively. The subscripts "st", "sf", and "ns" stand for the total, far-field, and near-field scour depths, respectively.

Bridge Piers	**R** (Pier 4)	**M** (Pier 3)	**L** (Pier 2)
	$\mathbf{D}_{st}$ | $\mathbf{D}_{sf}$ | $\mathbf{D}_{sn}$	$\mathbf{D}_{st}$ | $\mathbf{D}_{sf}$ | $\mathbf{D}_{sn}$	$\mathbf{D}_{st}$ | $\mathbf{D}_{sf}$ | $\mathbf{D}_{sn}$
1 (BR 9321 U/S Pier)	0.6 | 0.5 | 0.1	7 | 1 | 6	2.2 | 2 | 0.2
2 (BR 9321 Center Pier)	6 | 5 | 1	27 | 2 | 25	7 | 4.8 | 2.2
3 (BR 27801 D/S Pier)	25 | 20 | 5	18 | 8 | 10	30 | 15 | 15

As shown in Table 4, the bridge piers M2, M3, R3, and L3 would experience the maximum scour depths of 27 ft., 18 ft., 25 ft., and 30 ft., respectively. For details of the duration and location of these maximum scour depths see Tables 2 and 3.

6. Coupled flow and morphodynamics simulation of 500-year flood

6.1. Far-field simulation

In order to simulate the far-field domain we employed a background grid system with about 102 million computational grid nodes and river bed is meshed with over 140,000 unstructured triangular cells. The spatial and temporal resolution of computational grid system for this simulation is roughly similar to that of the 100-year flood. We first simulated the flow field for the 500-year flood (without sediment transport module activated) to reproduce a fully developed turbulent flow and suspended sediment load distribution in the entire study reach. After about one flow-through time (i.e. the duration of time it takes for a water particle to travel along the study reach) the fully turbulent flow is developed and thus we save the flow and suspended sediment concentration field as the initial boundary condition of the 500-year flood. For more details on the flow characteristics of the 500-year flood the reader is referred to the quarterly report of this project for the period of January 14, 2015 to March 15, 2015 in Appendix II of this report.

Starting from an initial bed morphology that was provided by sonar measurements of MnDOT, we continued the coupled flow and morphodynamics simulation for about 6 days. We note that it is highly unlikely that a 500-year flood continues for 6 days, however, in this study we investigated an extreme condition under which the 500-year flood continues at its peak discharge for 6 days. We plot in Figure 14 snapshots of the simulated flow field at the water surface. Like the case for the 100-year flood, development of scour hole geometry around bridge piers renders the bed geometry highly complex, which in turn modified the flow field downstream of the bridge piers (see Figure 14).

Compared with the 100-year flood, the velocity magnitudes at the water surface for the 500-year flood are slightly higher (see Figs. 4 and 14). It is important to note that the velocity magnitude at the beginning of the flood (t=0) is about 30 percent lower than that of the t=6 days, when the scour hole geometry near the bridge modified the overall flow pattern. This can be specifically seen in Figure 14(C) in a region between bridge and about 300 meters upstream of it, where the flow velocity at t=6 days reaches a maximum of ~3.2 m/s. This increase in flow power and turbulence might have several important implications for the stability of the river banks in this zone. We also note that a similar phenomenon was observed for the 100-year flood in which the flow velocity at t=6 days reaches a maximum of ~2.9 m/s.

As for the maximum scour depth near each bridge pier, we probed the time series of the simulated bed elevation at various local points around each bridge pier. Subsequently, the local point with the maximum scour depth is selected for each pier.

In Figure 15 we plot the time series of the scour depth at the local point of each bridge pier under the 500-year flood event. The naming of the bridge piers is as illustrated in Figure 7. As shown in Figure 15, the three bridge piers at the most downstream locations (L3, M3, and R3) experience the maximum scour depth.

We note that the time period of 6 days is not enough for the large-scale dunes to pass though the bridge pier site. This is why we do not observe the footprints of large-scale dune movements in Figure 15, as we did in Figure 8 for the 100-year flood event. We in Figure 8 show the bed evolution of the river bed for about 20 days, which is long enough for large-scale dunes to pass though the bridge site. Nevertheless, some small-scale dune migration (with an amplitude of about one foot) can be seen in the times series shown in Figure 15.

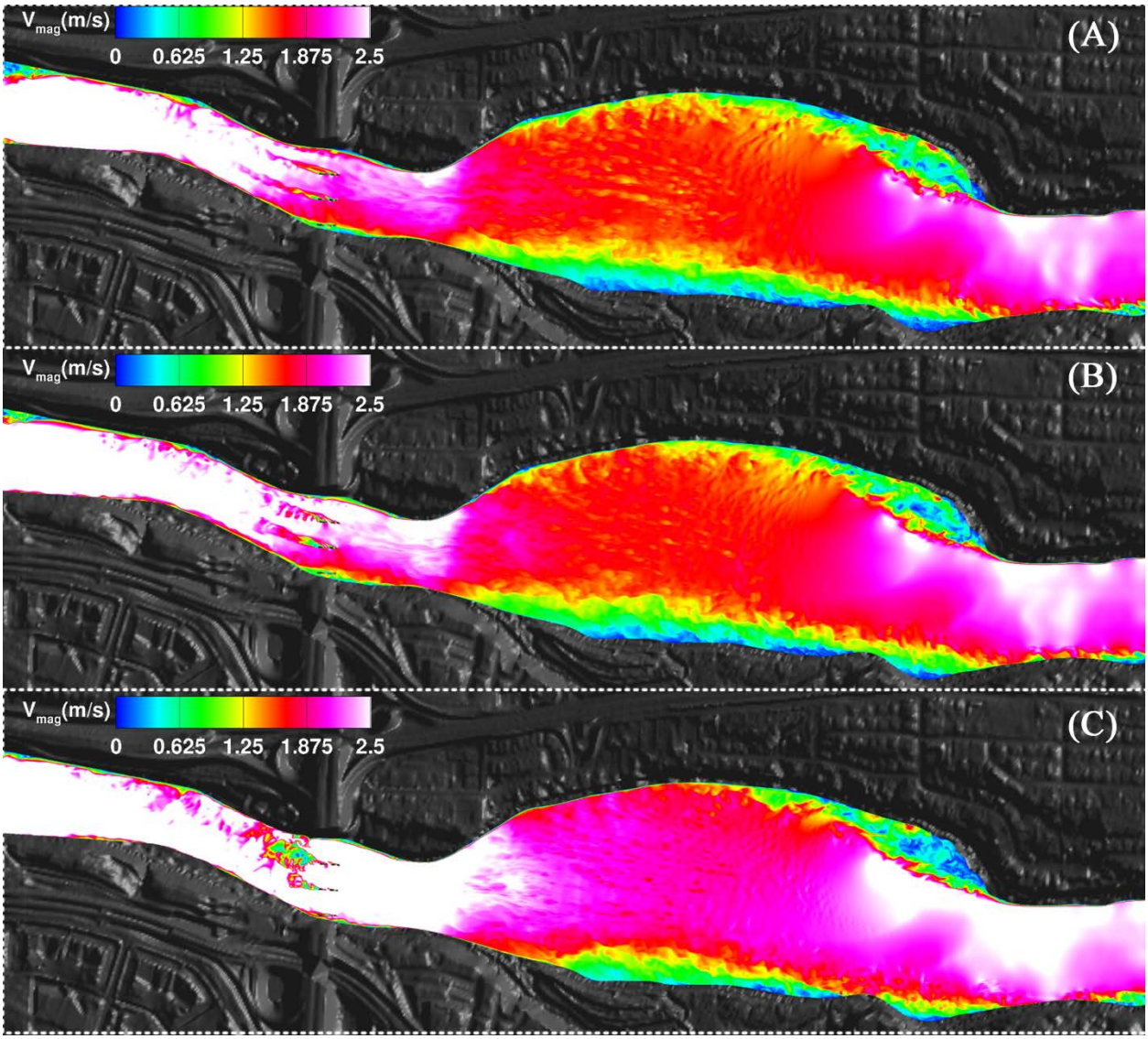

Figure 14: Snapshots of simulated flow field (velocity magnitude) at the water-surface over a deforming bed morphology (coupled simulations) after (A) t=0, (B) t=3 days, and (C) t=6 days. Flow is from right to left. Note that at t=6 days in (C) the scour hole geometry becomes significantly complex and deep, which in turn renders the flow highly turbulent.

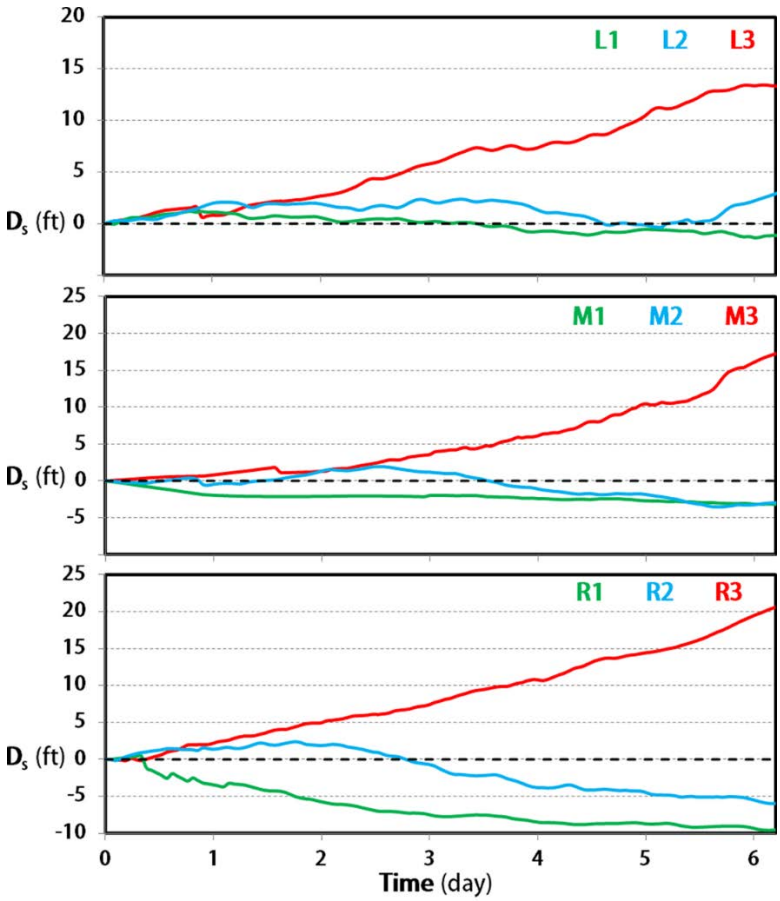

Figure 15: Far-field simulated time series of scour depth (D_{sf}) around each bridge pier at the local point with the maximum scour depth for the 100-year flood event.

In Table 5 we present a summary of the maximum scour depth at a local point around each bridge pier along with the duration of time that the maximum scour depth persists for the far-field simulation of the 500-year flood event. The locations of the maximum scour depths around each pier for the 500-year flood in the far-field simulation are similar to those of the 100-year flood.

Table 5: Summary of simulated maximum scour depth near each bridge pier (see also Figure 7 for bridge pier identity) under 500-year flood event in the far-field simulation. D_{sf} is the maximum scour depth at a local point around the pier, third column is the location of the local point around the pier, and the fourth column is the maximum time during which the pier experiences the maximum scour depth at the local point. The fourth column, the duration of scour depth, is based on the assumption that the 500-year flood continues for 6 days.

Pier	D_{sf} (ft.)	Location	Duration
L1	2.2	West side	~ 2 days
L2	3.4	West side	~ 3 days
L3	13.6	East side	~ 1 day
M1	0.1	Near downstream end	~ 0.1 day
M2	2.4	East side	~ 1 day
M3	17.5	West side and near downstream end	~ 0.5 day
R1	1.1	Near downstream end	0.1 day
R2	2.5	West side and near downstream end	~ 2 days
R3	21.1	West side and near downstream end	~ 0.1 day

6.2. Near-field simulation

For the near-field simulation of the 500-year flood event we first developed a fully turbulent flow over the entire near-field region and used it as an initial condition for the flow field. The coupled hydro-morphodynamics simulation of the near-field area was then performed for 5 days on a grid system with higher resolution (by a factor of ~2) than the far-field case to better resolve the energetic eddies that are responsible for local scour around individual bridge piers. The procedure we used in this simulation was the same as the near-field study of the 100-year flood case.

At the end of the near-field simulation we used the simulated time series of scour depth development around individual bridge piers, in addition to the far-field scour depth, to obtain the overall scour depth adjacent to each bridge pier. Details of the maximum scour depth for each individual bridge pier for the 500-year flood are shown in Table 6, where we summarize the simulations results of far-field and near field. Like the case for the 100-year flood, the total maximum scour depths in Table 6 are calculated by simply summing the maximum scour depths from far- and near-field simulations.

Table 6: Summary of simulation results for maximum scour depth (in ft.) near each individual bridge pier (see also Figure 7 for bridge pier identity) under 500-year flood condition. Dst, Dsf, and Dsn represent the maximum total scour depth, far-field scour depth, and near-field scour depth (in ft.), respectively. The subscripts "st", "sf", and "ns" stand for the total, far-field, and near-field scour depths, respectively.

Bridge Pier	**R** (Pier 4)	**M** (Pier 3)	**L** (Pier 2)
	$\mathbf{D}_{st}$ | $\mathbf{D}_{sf}$ | $\mathbf{D}_{sn}$	$\mathbf{D}_{st}$ | $\mathbf{D}_{sf}$ | $\mathbf{D}_{sn}$	$\mathbf{D}_{st}$ | $\mathbf{D}_{sf}$ | $\mathbf{D}_{sn}$
1 (BR 9321 U/S Pier)	2.4 | 1.1 | 1.3	7 | 0.1 | 6	2.5 | 2.2 | 0.3
2 (BR 9321 Center Pier)	5.1 | 2.5 | 2.6	26.2 | 2.4 | 23.8	6.2 | 3.4 | 2.8
3 (BR 27801 D/S Pier)	28.3 | 21.1 | 7.2	26 | 17.5 | 8.5	28.1 | 13.6 | 14.5

According to the Table 6, for the 500-year flood, the bridge piers M2, M3, R3, and L3 will experience the deepest scour depth of 26.2 ft., 26 ft., 28.3 ft., and 28.1 ft., respectively. This means that these are the bridge piers that will experience the maximum scour depths. This finding is similar to that we found for the 100-year flood. The magnitudes of maximum scour depths obtained for the 500-year flood are approximately similar to those we found for the 100-year flood event. However, we note that these scour depths in the 500-year flood occur in a time span of 5 to 6 days, while for the 100-year flood the maximum scour depth occur during a longer period of time of about 15 to 20 days.

7. Conclusions and final remarks

We simulated the coupled flow and bed morphodynamics of the Mississippi River in a 1.7 mile study reach, which covers 1.2 miles upstream to 0.5 mile downstream of the I-694 Bridge, under two flood events with 100- and 500-year return periods. The geometrical model of the river bathymetry, islands, and hydraulic structures used in the simulations are obtained from a combination of airborne LiDAR, sonar and standard surveying methods. ADCP measured flow field data under base-flow condition are employed to validate the simulation results of the model.

The coupled hydro-morphodynamics simulations for the 100-year flood event was continued for more than two weeks during which different bridge piers experience disparity of scour depth and sediment depositions. These simulations revealed that, under the 100-year flood event, the bridge piers 2, 3, and 4 of BR 27801 D/S Pier and piers 3 and 4 of BR 9321 Center Pier will experience the maximum scour depths of up to 30 ft. (see the executive summary and Table 4 for the quantitative results).

The coupled hydro-morphodynamics simulations for the 500-year flood event was carried out for about a week of physical time and the simulation results at their quasi-equilibrium revealed that the bridge piers 2, 3, and 4 of BR 27801 D/S Pier and Piers 2, 3, and 4 of BR 9321 Center Pier will experience the maximum scour depths of up to 28 ft. (see the executive summary and Table 6 for the quantitative results).

8. References

Baranya, S., Olsen, N. R. B., Stoesser, T., and Sturm, T. W. (2013). "A nested grid based computational fluid dynamics model to predict bridge pier scour." *Water Management*, 167(WM5): 259-268.

Kang, S., Lightbody, A., Hill, C., and Sotiropoulos, F. (2011). "High-resolution numerical simulation of turbulence in natural waterways." *Advances in Water Resources,* 34(1): 98-113.

Kang, S., and Sotiropoulos, F. (2011). "Flow phenomena and mechanisms in a field-scale experimental meandering channel with a pool-riffle sequence: Insights gained via numerical simulation." *Journal of Geophysical Research*, 116(F3).

Khosronejad, A., Kang, S., Borazjani, I., and Sotiropoulos, F. (2011). "Curvilinear immersed boundary method for simulating coupled flow and bed morphodynamic interactions due to sediment transport phenomena." *Advances in Water Resources,* 34(7): 829-843.

Khosronejad, A., Kang, S., and Sotiropoulos, F. (2012). "Experimental and computational investigation of local scour around bridge piers." *Advances in Water Resources,* 37: 73-85.

Khosronejad, A., Hill, C., Kang, S., and Sotiropoulos, F. (2013). "Computational and experimental investigation of scour past laboratory models of stream restoration rock structures." *Advances in Water Resourcesces.* 54: 191-207.

Khosronejad, A., Kozarek, Jessica L., and Sotiropoulos, F. (2014a): "Simulation-based approach for stream restoration structure design: model development and validation"F, *Journal of Hydraulic Engineering*, 140(7): 1-16.

Khosronejad, A. and Sotiropoulos, F. (2014b). "Numerical simulation of sand waves in a turbulent open channel flow." *Journal of Fluid Mechanics*, 753: 150-216.

Khosronejad, A., Kozarek, J. L., Palmsten, M. L., and Sotiropoulos, F. (2015). "Numerical simulation of large dunes in meandering streams and rivers with in-stream structure." *Advances in Water Resources,* 81: 45-61.

Merkuryeva, G., Merkuryev, Y., Sokolov, B. V., Potryasaev, S., Zelentsov, V. A., and Lektauers, A. (2015). "Advanced river flood monitoring, modeling and forecasting." *Journal of Computational Science*, 10: 77-85.

Nagata, N., Hosoda, T., Nakato, T., and Muramoto, Y. (2005). "Three-dimensional numerical model for flow and bed deformation around river hydraulic structures." *Journal of Hydraulic Engineering*, 131(12): 1074-1087.

Olsen, N. and Kjellesvig, H. M. (1998). "Three dimensional numerical flow modeling for estimation of maximum local scour depth." *Journal of Hydraulic Research*, 36(4): 579-590.

Toso, J. W. (1993). Bridge scour investigation, bridge and Interstate highway over the Mississippi river. Minnesota Department of Transportation, St. Paul, MN.

Appendix A: Quarterly Report 3/15/15 – 6/15/15

QUARTERLY PROGRESS REPORT

to the

MINNESOTA DEPARTMENT OF TRANSPORTATION (MNDOT)

on Project T9T064
Three-Dimensional (3-D) Simulation of Bridge Foundation Scour Mississippi River Bridge 9321 & 27801

for period

March 15, 2015 to June 15, 2015

Dr. Fotis Sotiropoulos (PI)
St. Anthony Falls Laboratory
University of Minnesota

Research Approach

The objective of this research is to develop comprehensive quantitative numerical model of flow and sediment transport (bed and suspended load transport) in the Mississippi river where is intersects bridge 9321 of interstate I694. The simulation domain includes about 1.2 miles of the river upstream of the bridge piers, all of bridge piers (at I694), and 0.5 mile of the river downstream of the bridge. First phase of the project consisted of collection of bathymetry and flow field data that is carried out by MnDOT personnel and successfully transferred to SAFL research team. The important part of the data transfer from MnDOT to SAFL was to ensure that the measured bathymetry and ADCP (flow measurements) data match correctly with existing LiDAR data for the study area.

Progress during Reporting Period

In order to start the simulation we first need to reconstruct the boundary conditions including:

1) Analysis of flow measurement data on the 5th of May 2014
2) Statistical analysis of flow structure on the 5th of May 2014
3) Analysis of scour/degradation of bed elevation from 2009-2014
4) Simulation of suspended sediment transport under 100-year flooding condition

The measurement on May 05 2015

A separate campaign has been carried out on May 5th 2015 to investigate the flow at the confluence under low flow condition using two measuring method: i) moving-boat method and ii) fixed-boat method. The field survey is following the standard USGS procedure for large scale rivers. The ADCP (RDI Rio Grande 1200Hz) is used to provide depth using bottom tracking mode at every cross-section. The ADCP is set to pulse (or ping) at frequency of 2Hz. Four beams of ADCP are setup at 20-deg angle. The bin size is chosen to be 50 cm with the accuracy in velocity measurement is 1 mm/s. The ADCP is tethered to the main motored boat using a separated composite boat with the antenna of its GPS right above the ADCP at the fixed depth of 0.061m to the water surface. Otherwise noted the measurements units (velocity, depth) are set to be in SI system. The earth projection system is converted to be UTM-15N.

Two cross-sections M1 and M2 are chosen to perform such a measurement as shown in Figure 2. Cross-section M1 lies closer to the upstream junction corner of the island and the cross-section M2 is chosen to be close to the bridge. In addition, a single-point measurement is also chosen between M1 and M2 as seen in the figure.

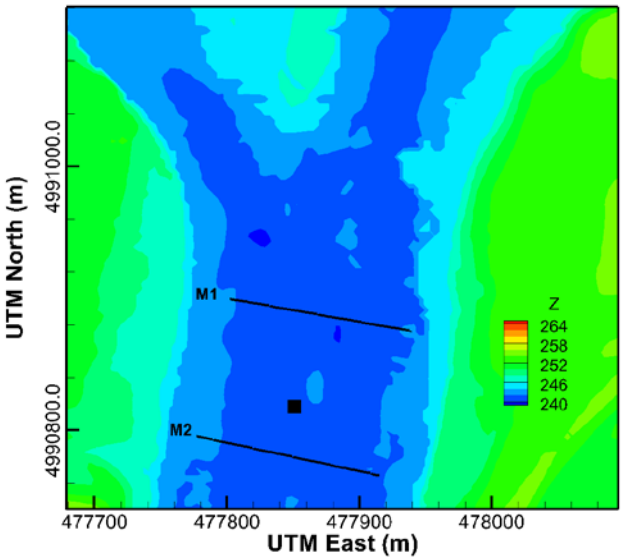

Figure 1: Two cross-sections (M1 and M2) of the measurement on May 5th, 2015 using moving-boat method and a single point (filled rectangle) measurement using fixed-boat method.

On cross-section M1 and M2, standard USGS method for measuring discharge is carried out. Four successive transects are obtained at each cross-section. During one-transect, the location of the moving-boat is monitored using the online GPS tracking that helps the boat to traverse within a controllable range. During the fixed-boat method, the ADCP data is constantly saved in about 10-15 minutes in one setting to prevent data loss.

The flow depth in the confluence is about 2m maximum and becomes shallow around 0.5m in the upstream branches. The average velocity is about 0.5m/s and consistently over the time. The flow splitting and the merging interface is clear to see from the ADCP data. We hit the rock in the interface region which indicates the line of rock as anticipated is real. The discharge measurement from the station USGS 05288500 MISSISSIPPI RIVER AT HWY 610 IN BROOKLYN PARK, MN is Q=157.72 CMS.

Point measurement using fixed-boat method

Since the boat is anchored to the bed its motion is limited horizontally within 2m as the GPS tracking data shown in Figure 2. On the vertical viewpoint the boat provides a small window of 3m within the water column as seen in Figure 3. The vertical resolution is set in the ADCP to be 0.5 m with the acquisition frequency of 2Hz. spatial average between the measured points give the flow velocity around 0.5 m/s.

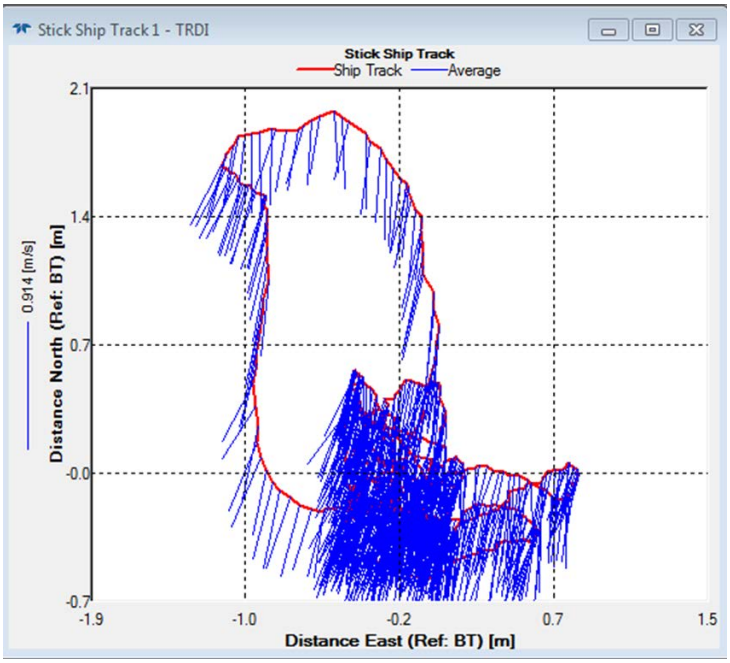

Figure 2: Horizontal location of the boat during measurement at the chosen fixed-location.

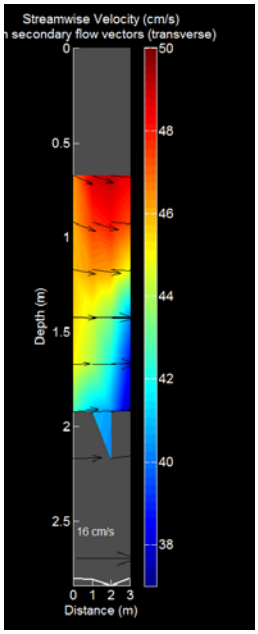

Figure 3: Vertical velocity profile at the measured point.

The fixed-boat method gives the time series as shown in Figure **3**. The velocity components change quickly in time and vary largely from 30 cm/s to 80 cm/s. The turbulent fluctuation is significant during the period of measurement. From Figure 4 it can be inferred that there exists a large scale structure presenting between cross-section M1 and M2.

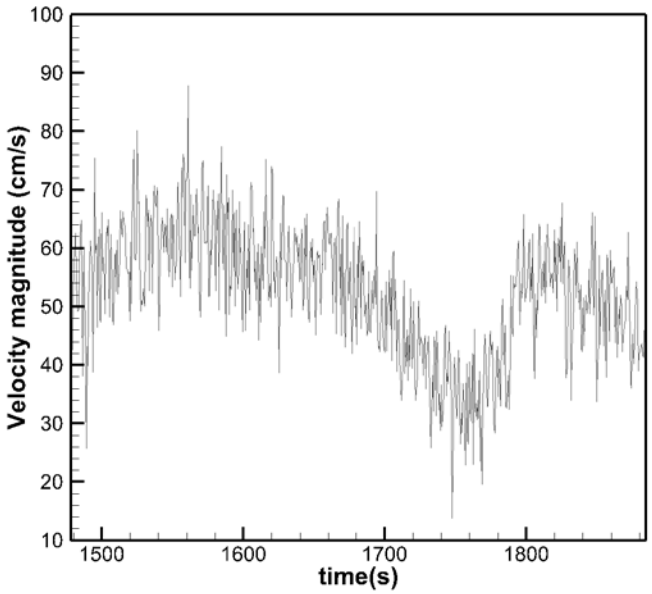

Figure 4: Time series of instantaneous velocity magnitude at the point of measurement using fixed-boat method.

Since the total time of measurement at the point is large (30mins) it is possible to produce the time-averaged velocity profile along the depth as shown in Figure 5. Our data, however, does not show that the flow follow closely log-law (the solid line). These results suggest that the flow is not fully developed and the interaction between flow and the bed topography is significant that changes the time-averaged flow structure.

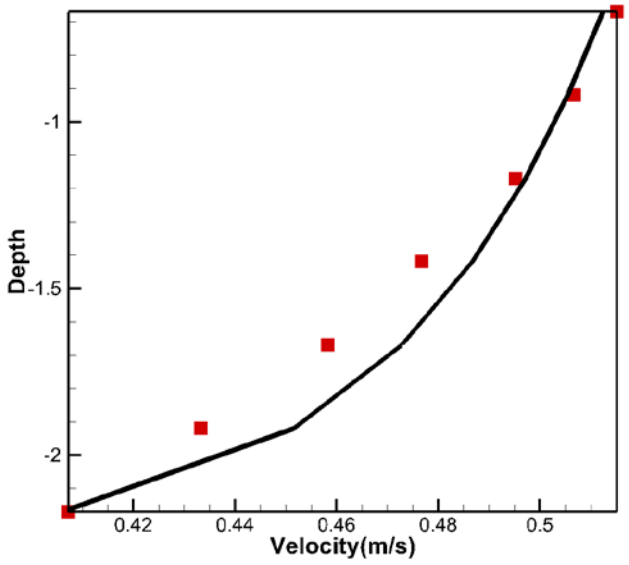

Figure 5: Time-averaged velocity profile at the point of measurement. Solid line represents log-law distribution.

We also calculate the distribution of Turbulent Kinetic Energy (TKE). It is shown that the TKE follows closely the expected trend where the highest values of TKE are distributed close to bed. Here the TKE drop quickly from 100 cm^2/s^2 to 80 cm^2/s^2 near the water surface suggesting that the large scale turbulent structure presents strongly on the water surface.

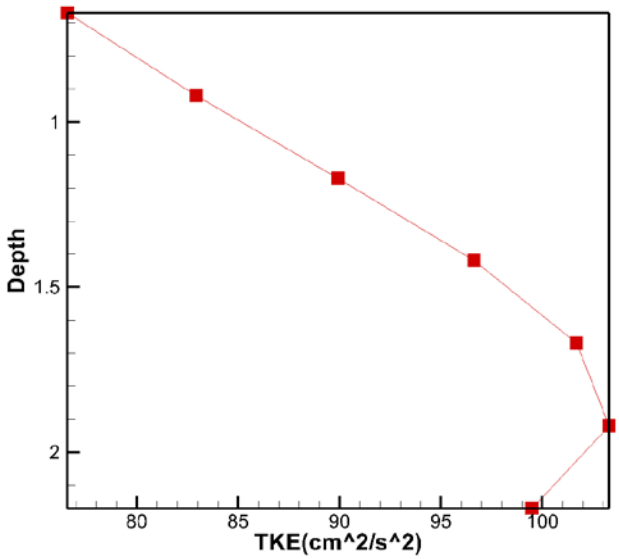

Figure 6: Distribution of Turbulent Kinetic Energy along the depth.

Three-dimensional flow structure at the confluence

Here we utilize the automated software (Velocity Mapping Tool; https://hydroacoustics.usgs.gov/movingboat/VMT/VMT.shtml) for analyzing the dataset from ADCP measurement. The software extracts the velocity field from the cross-section and projects the available data on the ship tracks to the straight cross-section. The advantage of using VMT is the ability to extract three-component velocity distribution on a cross-section.

We also write an in-house MATLAB code to extract the ADCP data from the ASCII Classical Output file. Our in-house code is able to extract the pointwise data along the depth to provide the description of three-dimensional velocity field as shown in four successive transects at cross-section M1 as shown in Figure **7**. Since 4 transects are not exactly overlapped due to the inconsistency in the boat tracks we obtain different instantaneous velocity profiles.

Four transects all provide similar description of the velocity distribution. There exist main two high areas with large velocity magnitude close to the left and right banks. The largest velocity magnitude in this case is about 80 cm/s. There exists also a distinct mixing interface between these two jets denoting by the very low velocity magnitude close to the center of the channel. The existence of this mixing interface is consistent in all transects suggesting that its location is rather stable throughout the measurement period (20 minutes for 4 transects).

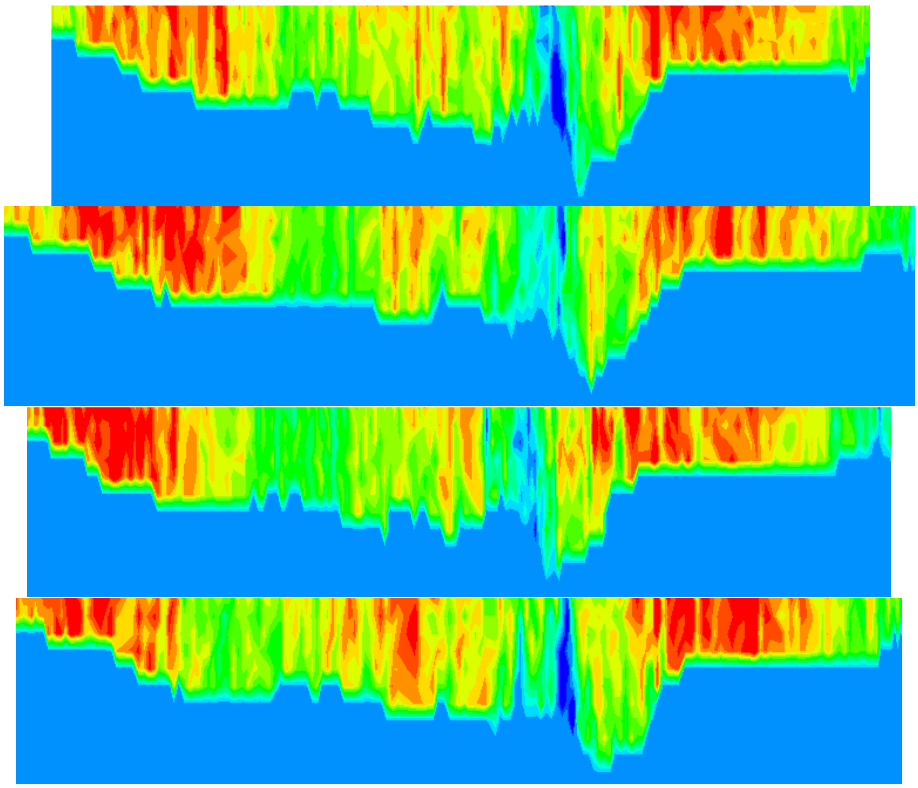

Figure 7: Distribution of velocity magnitude at different transects at cross-section M1 (4 transects).

The largest changes occur at the center of the channel where a dynamic region of flow velocity alternates with time. In order to provide the averaged value for M1, an averaging transect for M1 is interpolated from the 4 transects using VTM software that provides the result in Figure 8. The velocity profile indicates that a fast mixing process appear in this shallow region with the velocity magnitude varies from 20 cm/s to 60 cm/s.

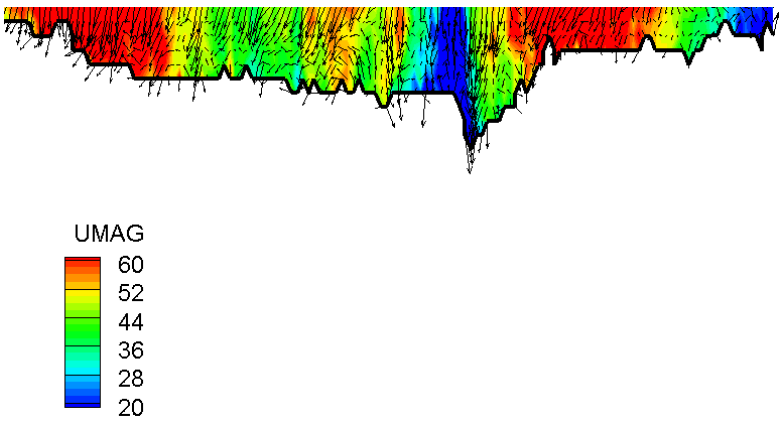

Figure 8: The average velocity distribution using the data from 4 transects.

The measured data for cross-section M2 is shown in Figure **9**. In this cross-section, two jets are found with high velocity cores are found at different transects. However, the jet's core near the west bank is significantly higher than the one on the east bank. One important factor can be seen here that the mixing interface does not exist in this case.

Comparing the measured data on the cross-section M1 and M2 indicates that the flow structure in these cross-sections is rather stable throughout the measurement period (20 min). However, the variability (statistics) of the fluctuation between the transect (ensemble) differ strongly from one to the other. There is no reverse flow on the east side near the east bank suggesting that such circulation structure occurrence depends on the specific discharge and flow depth.

It is important to the note that there exists a strong flow near the MI (at the center of M1). Such strong flow and its large variability indicate that it is a large coherent structure that sheds from the island upstream. Another important factor is the high velocity core near the west bank, which is significantly high and is pushed toward the west bank. This is not common since flow is expected to converge to the center of the channel as usual cases. The distance between the two velocity cores are two far indicating that the mixing layer has spread. From the cross-section flow pattern of M1 and M2, it is shown that the existence of the mixing interface is an important characteristic phenomenon that should be included in the analysis.

Large scale flow structure on two measured cross-sections

In order to provide the description of the flow structure in the confluence, depth-averaged velocity is calculated from the ADCP data and presented in Figure 11. The measurement on the profiles on M1 and M2 shows that the flow at the M1 cross-section has the triple jet structure. In addition to the normal double-jet structure as seen in 31st Jul 2014, there exists a clear additional jet near the center of the channel with the peak velocity around 50cm/s. This jet has a distinct separation from the east tributary jet, which has the sharp interface mixing location. The jet at M2 location however shows that the two jets already mixed and the distinction between the two profiles has disappeared.

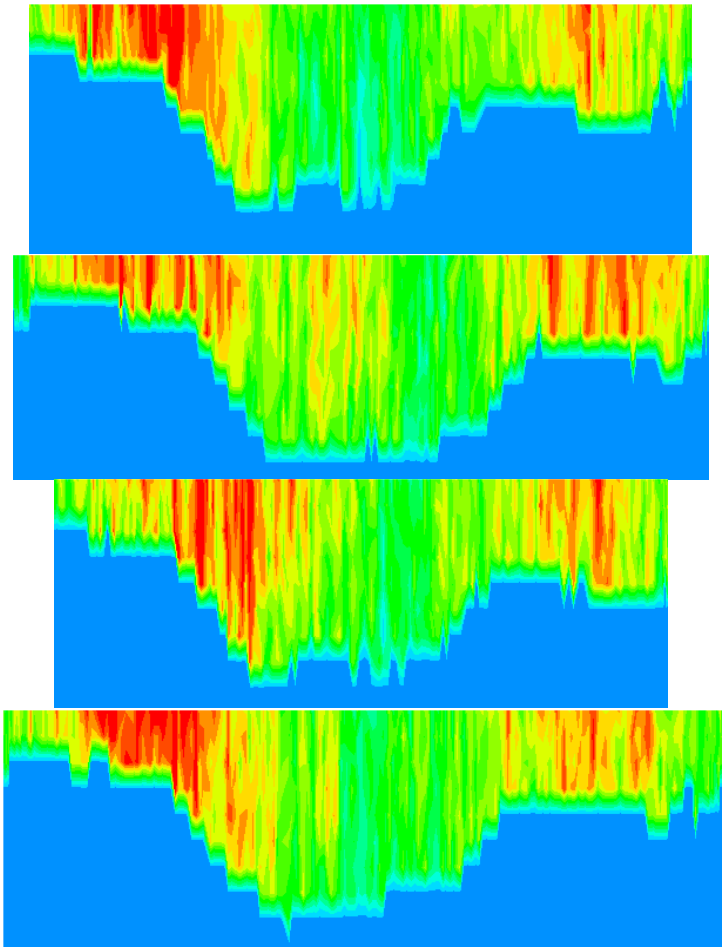

Figure 9: Contour of velocity magnitude and velocity vectors at cross-section M2 at four transects.

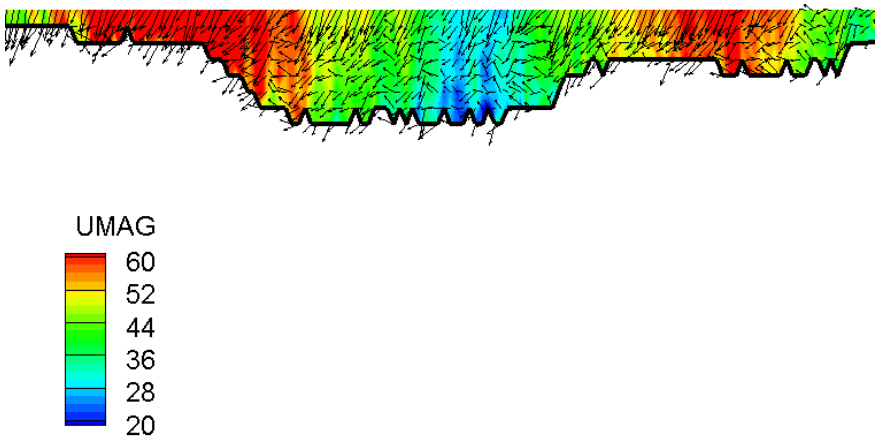

Figure 10: The averaged velocity profile calculated from four transects at cross-section M2.

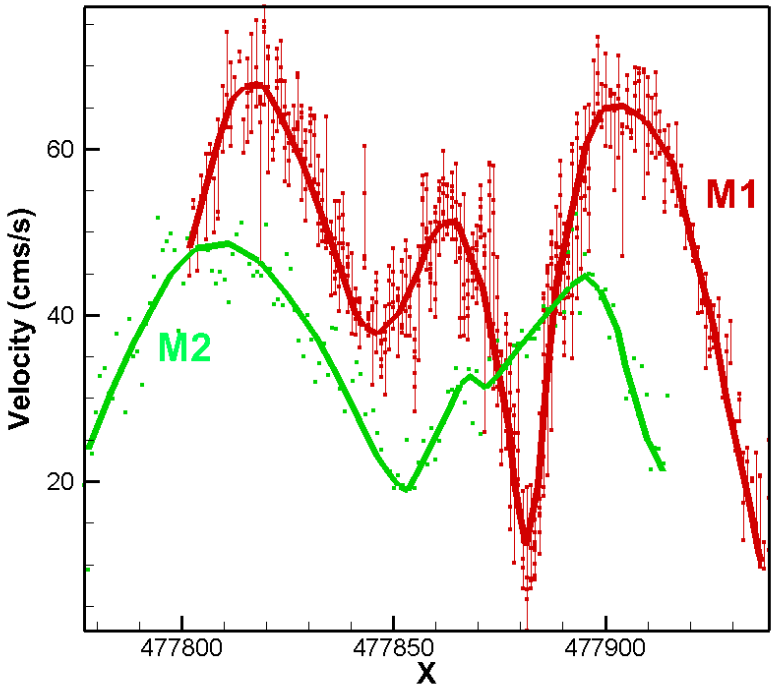

Figure 11: Depth-averaged velocity profiles at cross-section M1 and M2.

In contrast to cross-section M1, a strong mixing interface does not exist in the cross-section M2. Overall, the cross-section is well mixed showing high level of turbulence across the cross-section.

The statistical analysis of the hydrodynamic data on May 5th 2015

The probability distribution function of the streamwise velocity components on the surface is calculated from the time series measurement. The result indicates that the streamwise component here do not exhibit double-peak structure. In fact, the single peak of probability density function on the measurement point indicates that the flow velocity is similar to fully develop channel flow where the mixing is complete right after the cross-section M1.

The evolution of bed elevation from 2009-2014

We compared the recent measured bathymetry data (2014) with an older one (2009) and our analysis also showed that there exists large rocks (~0.5 m in diameter) in both data (see Figure 12 on the thalweg of the main channel). However, the location of these rocks is slightly different between the bathymetry maps in the rock lines suggesting that the rocks move during this period.

There exists a consistent degredation of the 2014 thalweg comparing to 2009 thalweg as shown in Figure 12. Interestingly, we observe that the thalweg on the west tributary is significantly higher (1m) than that on the east tributary. Such trend does not hold in the confluence region, especially further downstream where this trend reverses suggesting that there exists a switch in the degradation dynamics in the confluence from one tributary to the other.

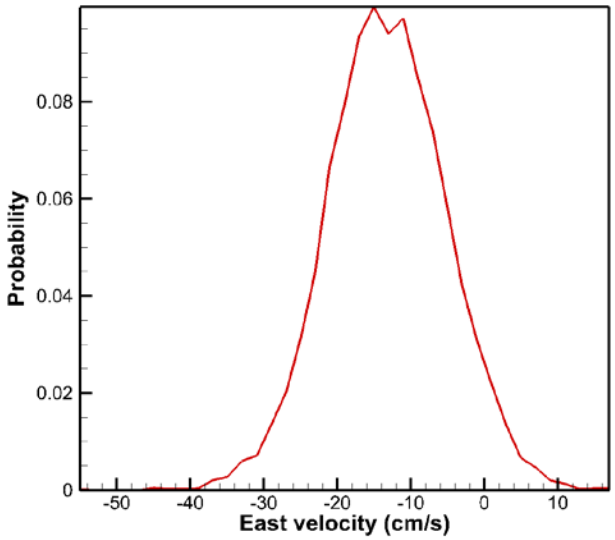

Figure 12: Probability density function of streamwise velocity component on the surface at the measured point.

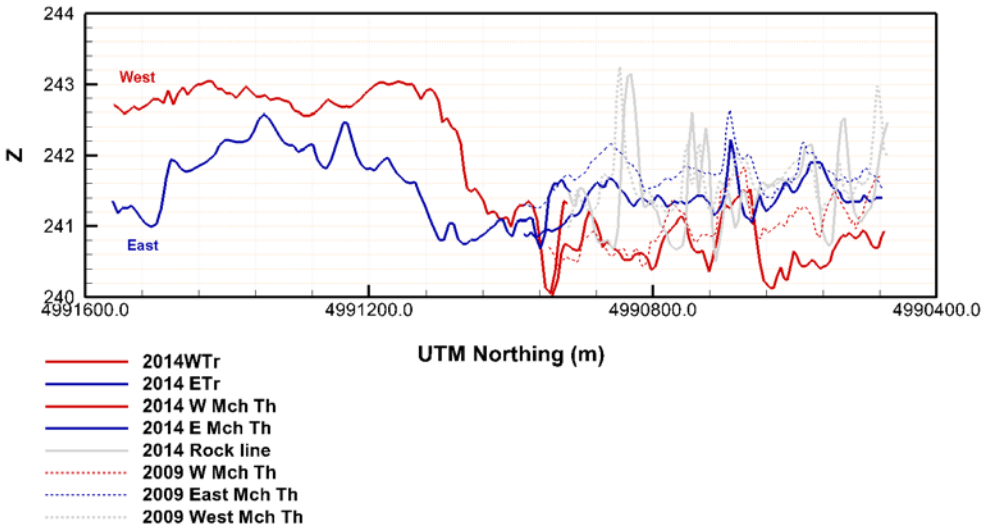

Figure 13: The thalwegs of both tributaries in 2009 and 2014.

Two cross-sections are chosen to monitor the degradation as seen in Figure 13 and Figure 14. From these figures, it shows that the scour pool only extends to the cross-section close to the confluence and is shifted to the west side of the main channel. The extension of the scour pool is pushed more toward the east tributary. The largest scour can be observed in both figures is less than 1m.

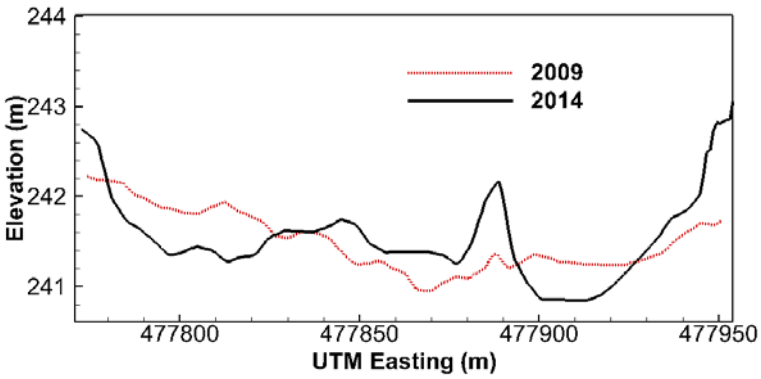

Figure 14: Cross-section 7 (the 31st July 2014).

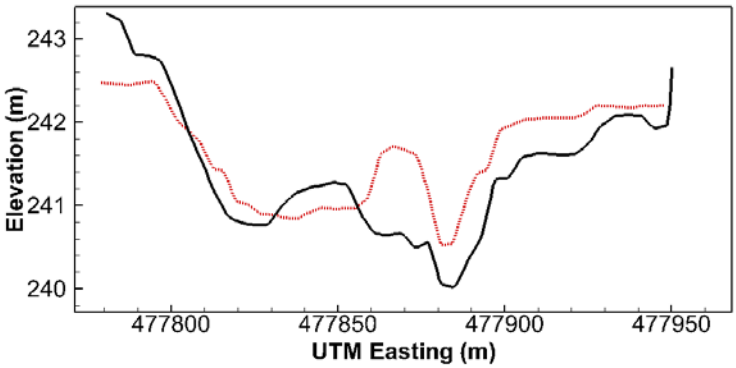

Figure 15: Cross-section 9 (the 31st July 2014).

Suspended sediment concentration field in the large scale domain

We successfully simulated the suspended sediment concentration field for the 100-year flood event within the study reach (large-scale domain). The simulated suspended sediment load is being incorporated in hydro-morphodynamics (VSL3D) model to compute the sediment transport and river bed evolution within the reach. The simulation results for the bed elevation and scour depth in the river reach and adjacent to each bridge pier will be reported in the next quarterly report. Herein we only discuss the simulation results for suspended load for the 100-year flood event (100-YFE).

The 100-YFE in the Large-scale domain (LSD) is simulated on a computational grid system with about 94.2 million nodes. For the inlet boundary condition of suspended load, we used the five free-surface samples collected by MNDOT team. These raw data was analyzed in the SAFL and the suspended sediment concentration was determined to vary between 1.7×10^{-8} to 2.7×10^{-8} mg/l, which are insignificant. Thus, we expect the bed-material entrainment into the flow field to be the most important source of suspended load and that most of the suspended sediment load to be concentrated near the mobile-bed of the river. A sample of bed-load material collected by SAFL team near the bridge pier was analyzed to determine the gradation curve of bed material (see Figure 16). According to this analysis, the bed material in the study site has D_{50} and D_{90} of about 0.4 mm and 2.0 mm, respectively. We employed a flux pick-function (Khosronejad and Sotiropoulos, 2014) as the boundary condition of the suspended load on the mobile-bed to allow entrainment of bed material into the turbulent flow domain.

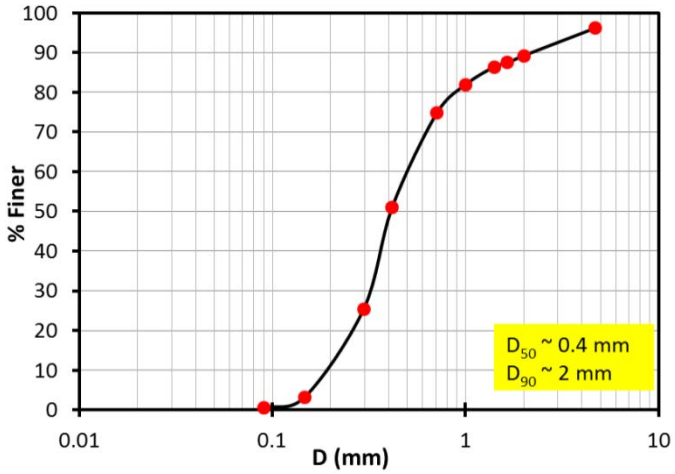

Figure 16: Gradation curve of the bed material at the study site.

In Figure 17 we show a snapshot of simulated suspended sediment concentration field for 100-YFE in the Large-scale domain (LSD) at time equal to 1.1 flow through, i.e. when the suspended sediment concentration field reached a quasi-equilibrium state. A flow through time is the duration of time that takes for a water particle to travel from inlet to the outlet of the study reach. As one can clearly see in Figure 17, for the most part of the study reach--upstream of the bridge piers--the suspended sediment concentration is high near the mobile-bed and significantly low near the free-surface (see Figure 17(A)-(B)). Presence of bridge piers (window (C) of Figure 17) increases the turbulence level in the water column, which directly leads to significant entrainment of the bed material, and consequently augments the suspended sediment concentration immediately downstream of the bridge piers (see Figure 17 (C)).

Farther downstream of the bridge piers, the suspended sediment materials--under the effect of their settling velocity--start to deposit. Thus, the suspended sediment concentration in the water column, once again, decreases (see Figure 17 (C)): reaching a typical vertical suspended sediment concentration profile. This is evident in the color map of suspended sediment concentration at the outlet cross-section in which the suspended sediment concentration near mobile bed is high, while the near free-surface concentration is close to machine-zero.

Conclusions

On the date of May 5th 2015 we show that the flow at the confluence is highly dynamics as two tributaries merge. Here due to the higher elevation of the bed on the east tributary, the water depth at the avalanche face is relatively low (0.5 m). Due to the low depth, the velocity at this avalanche face is accelerated and creating a fast jet over the top of the avalanche. This fast jet separates the flow into two portions with the fast jet with approximately peak of 70 cm/s. The jet of the west tributary also produces a fast jet of roughly 60cm/s. In the middle of two jets there exists a different jet, which we think it is the wake of the island (specifically under the effect of bed bathymetry). The central jet seems to disappear in cross-section M2 right after the point measurement section with two peaks of 50 cm/s. Thus the instantaneous flow at the surface and the plane near the bottom shows that there exists a large scale structure on the main channel. The existence of dynamic mixing interface does not exist beyond the cross-section M1. We also observe a significant degradation of bed elevation from 2009 to 2014 of this area. The bed elevation is roughly reduced maximum to 1m during this period.

Simulation results for the suspended sediment concentration field for 100-YFE in LSD show a typical vertical profile of the sediment concentration with high values near the bed (due to significant bed-material entrainment) and low values above half-depth of the river. This typical profile is interrupted by bridge piers and suspended sediment load immediately downstream of the bridge piers is significantly high (with an approximately even distribution of suspended sediment concentration in vertical direction).

Farther downstream of the bridge piers, the suspended sediment concentration field returns to its typical quasi-equilibrium distribution.

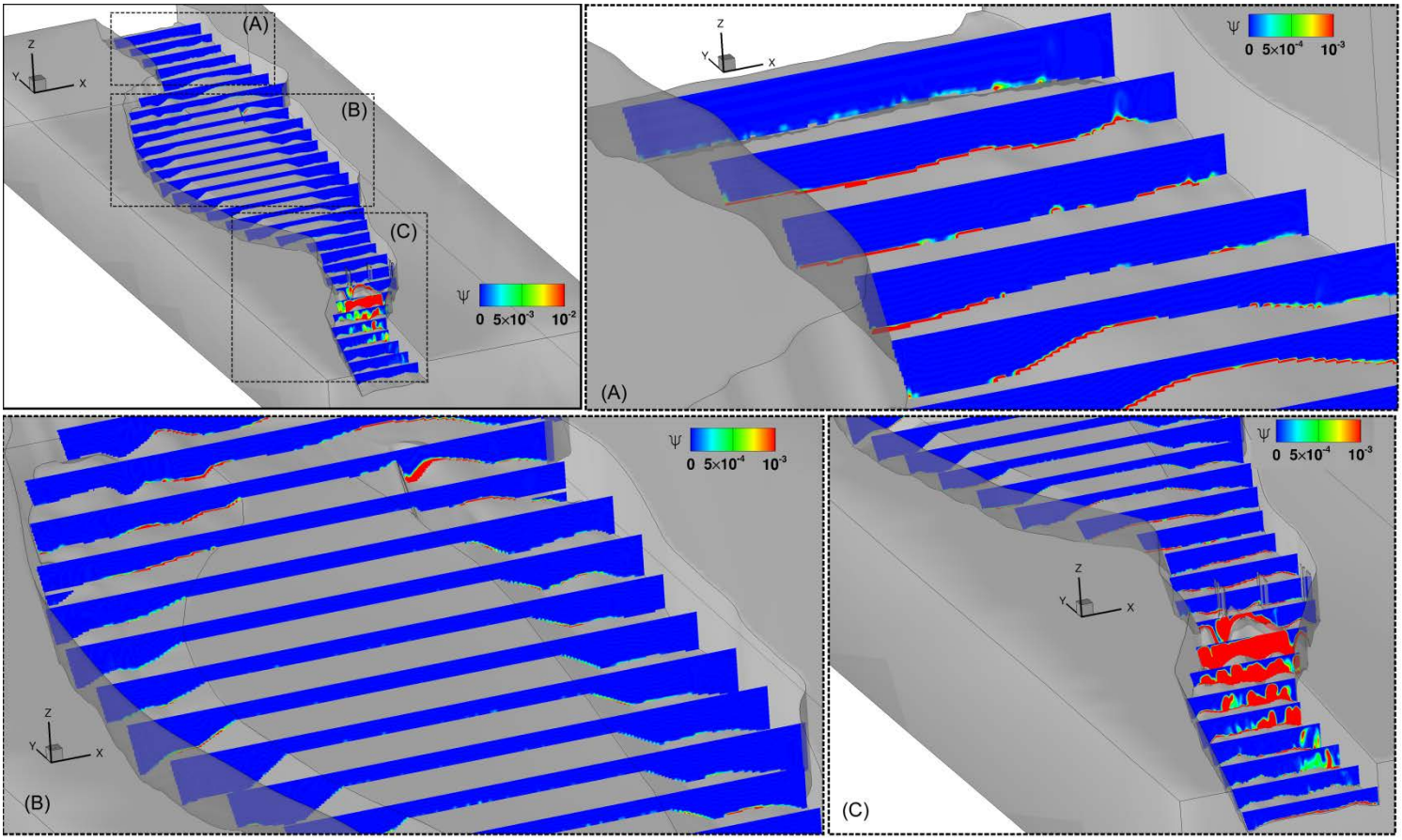

Figure 17: Color maps of simulated suspended sediment concentration (ψ) (in volume fraction) for 100-YFE in the LSD on 31 vertical cross-sections along the river at a time equal to 1.1 flow through. Windows (A), (B), and (C) show the zoomed-in of various regions shown in the top-left picture. Flow is from top to bottom.

References

Khosronejad, A., Kang, S., and Sotiropoulos, F. (2012), Experimental and computational investigation of local scour around bridge piers. *Advances Water Resources*, 37, 73-85, doi:10.1016/j.advwatres.2011.09.013.

Khosronejad, A., Hill, C., Kang, S., and Sotiropoulos, F., (2013), Experimental and computational investigation of local scour around in-stream restoration structures. *Advances Water Resources*, 57, 191-207, doi:10.1016/j.advwatres.2013.01.008.

Khosronejad, A. and Sotiropoulos, F. (2014), Numerical simulation of sand waves in a turbulent open channel flow, *Journal of Fluid Mechanics*, 753:150-216.

Toso, J. W., Bridge scour investigation, Bridge 9321 and 27801 Intestate Highway 694 over the Mississippi river in Hennepin County
, Minnesota Department of Transportation, 1993.

Appendix B: Quarterly Report 1/15/15 – 3/15/15

QUARTERLY PROGRESS REPORT

to the

MINNESOTA DEPARTMENT OF TRANSPORTATION (MNDOT)

on Project T9T064
Three-Dimensional (3-D) Simulation of Bridge Foundation Scour Mississippi River Bridge 9321 & 27801

for period

January 15, 2015 to March 15, 2015

Dr. Fotis Sotiropoulos (PI)
St. Anthony Falls Laboratory
University of Minnesota

Research Approach

The objective of this research is to develop comprehensive quantitative numerical model of flow and sediment transport (bed and suspended load transport) in the Mississippi river where is intersects bridge 9321 of interstate I694. The simulation domain includes about 1.2 miles of the river upstream of the bridge piers, all of bridge piers (at I694), and 0.5 mile of the river downstream of the bridge. First phase of the project consisted of collection of bathymetry and flow field data that is carried out by MnDOT personnel and successfully transferred to SAFL research team. The important part of the data transfer from MnDOT to SAFL was to ensure that the measured bathymetry and ADCP (flow measurements) data match correctly with existing LiDAR data for the study area.

In the next phase of the project, we will import the measured bathymetry and geometrical data of bridge piers into the VSL3D model to carry out flow and suspended sediment field simulation throughout the ~1.7 miles of the Mississippi river at the study site, for two flood events of 100 and 500 years. The VSL is a state-of-the-art 3D computational fluid dynamics (CFD) model developed at SAFL by PI Sotiropoulos that is capable of simulating real-life hydraulic engineering flows using advanced numerical techniques and turbulence models that can be coupled with turbulent free surface, and bed-morphodynamics modules (Khosronejad et al. 2012, 2013, 2014).

Once the flow field simulation is successfully carried out, the VSL3D model will be employed to carry out a fully coupled flow and sediment transport simulation for the two flood events. These fully coupled simulations will reveal the depth and extend of scour hole at the vicinity of each bridge pier for different flood events.

Progress during Reporting Period

In order to start the simulation we first need to reconstruct the boundary conditions including:

5) Spatial analysis of three-dimensional flow structure from ADCP
6) Preliminary simulation of the 31st Jul 2014 measurement
7) Grid sensitivity study

Analysis of data measurements

In order to compare with the simulation, the velocity data are required to be extracted from the MnDOT measurements. We integrate the different measurements at May 16th, June 13th, July 14th, and July 31st of 2014. The measurements of 13th of June provide mostly the velocity field near the upstream portion of the computational domain. The measurement of 14th of July provides the data for the left branch mostly near the bifurcation point. The measurement of 31st of July provides the data mostly in the bridge region. We will use this dataset in order to compare with the simulation. The measured data are depicted in Figures 12 and 13.

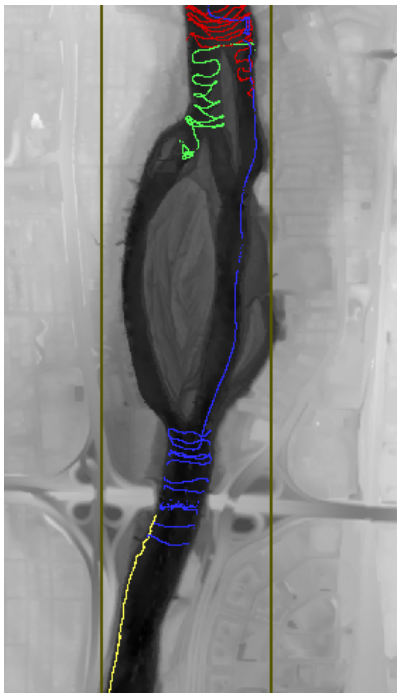

Figure 16: Velocity field measurements were carried out by ADCP along the colored lines: May 16th (yellow path), June 13th (red path), July 14th (green path), and July 31st (blue path) of 2014.

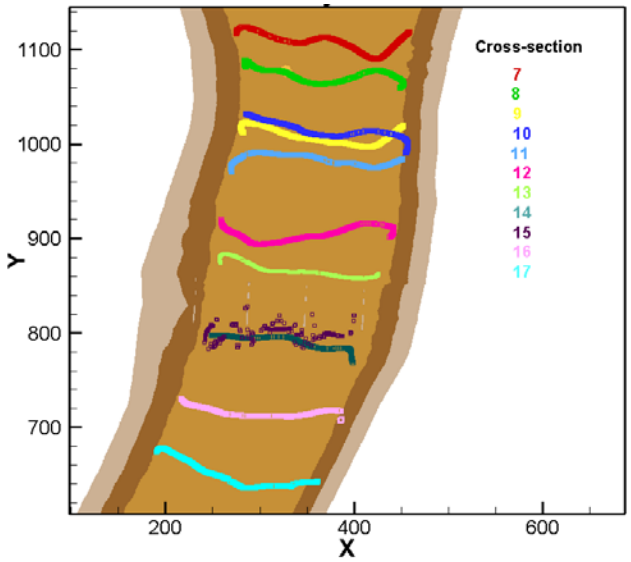

Figure 17: Different cross-sections for measurement of July 31st, 2014

As shown in Figure 3, the cross-sections adjacent to the bridges include 12, 13, 14, 15 and 16. From the depth-averaged velocity data, the interpolated velocity contour is shown in Figure 14 from the measurements. It shows that there are two jet-like flows from the confluence site to the bridge. The stronger jet is the right branch with the velocity is up to 1 m/s. An interesting observation is that the region near the bridge has an uneven distribution of velocity field as shown in Figures 15 and 16.

Measured data and preliminary assessments for numerical simulation

Measurements were carried out by MinDOT personnel on different days: i) the 16th of May 2014; ii) the 13rd of Jun 2014; the 14th of Jul 2014 and the 31st Jul 2014. In order to verify and check the validity of the

measurement, USGS measurement stations are chosen as USGS 05288500 MISSISSIPPI RIVER AT HWY 610 IN BROOKLYN PARK, MN shown in Table 1.

Table 1: Measured discharge and water elevation

Day	H-ADCP(feet)	Q-ADCP (cms)	Q-USGS(cfs)
16 May	809.01	910	40,000
13 June	807.6	1100	31,000
14 Jul	805.1	N/A	21,000
31 July	801.903	283	10000

The Reynolds number is defined as $Re = \rho UH/\mu$. Here U is the bulk velocity, H is mean flow depth, ρ is the water density, and μ is the dynamics viscosity of water (=10^{-6}m^2/s). The main computational parameters from measurements are shown in Table 2. The computational grids are structured grid with size shown in Table 3.

Table 2: Main parameters for different simulation scenarios

Case	Q(cms)	DH(m)	A (m^2)	Re	U	Grid	Mean Flow Depth (m)
31Jul	283	245-244.42	205	5.53e+6	1.38m/s	1,2,3	4m
16 May	850	246.5-246	800	4.25e+6	1.04	1,2,3	4m
100-year	2789.2	249.6- 249	1488 m^2	7.5e+6	1.87m/s	3	8m
500-year	3667	250.7-250.3	1760m^2	8.33e+6	2.083m/s	3	9.2m

Table 3: Computational grids for the computations

Grid name	**Grid Size ($\Delta x \times \Delta z \times \Delta y$)**	**Total**
1 - 201	401 × 41 × 601	10M
2- 301	801 × 61 × 1201	48M
3- 401	1501 × 61 × 1201	109M

Three-dimensional flow structure at the confluence

The low flow condition (31st July 2014) is the challenging problem since the low water elevation creates high flow speed in shallow areas. For the purpose of comparing the simulation results and the field

measurements we focus on the confluence area at the downstream point of Durham island. The subsets of the measurements are the cross-sections 7 to 17 in the vicinity of the bridges as shown in Figure 3 in the local coordinate system (SI units). The cross-sections 7 to 10 cover the confluence region where the mixing of left and right branches occurs. The cross-sections 11 – 17 locate at the downstream of the bridges. We, therefore, separate these cross-sections in two separate hydrodynamic regimes: i) confluence dynamics and ii) wake of the bridge piers.

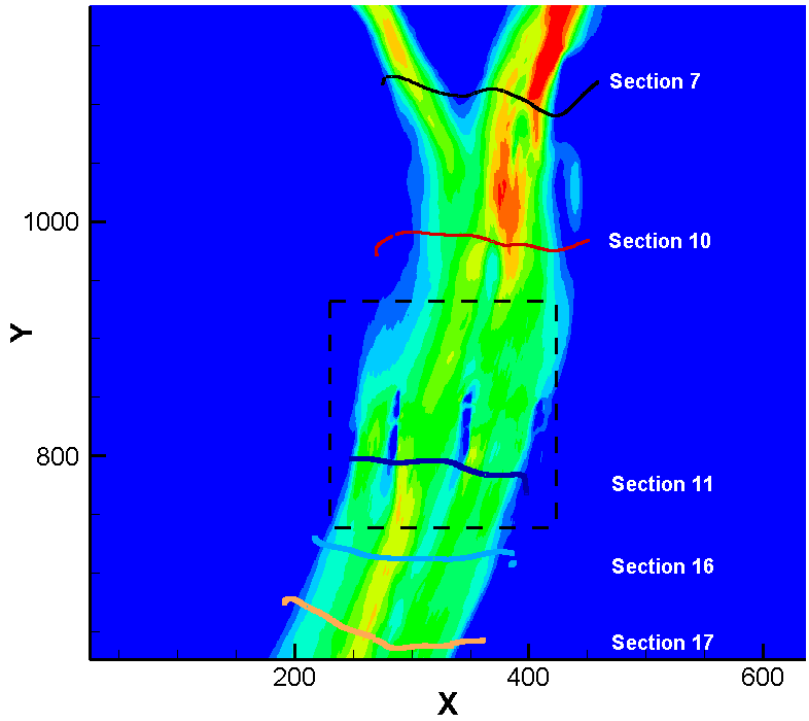

Figure 18: The plan layout of the measured cross-sections on the 31st Jul 2014. The bridge area is illustrated with the black dash-line.

Here we utilize the automated software (Velocity Mapping Tool; https://hydroacoustics.usgs.gov/movingboat/VMT/VMT.shtml) for analyzing the dataset from ADCP measurement. The software extracts the velocity field from the cross-section and projects the available data on the ship tracks to the straight cross-section as shown in Figure 4. Note that the boat's track deviates far from the straight line and there are significant portions of the cross-section are missing by this type of interpolation. The remedy can be feasible if multiple ship tracks are implemented along the same path. The advantage of using VMT is the ability to extract three-component velocity distribution on a cross-section.

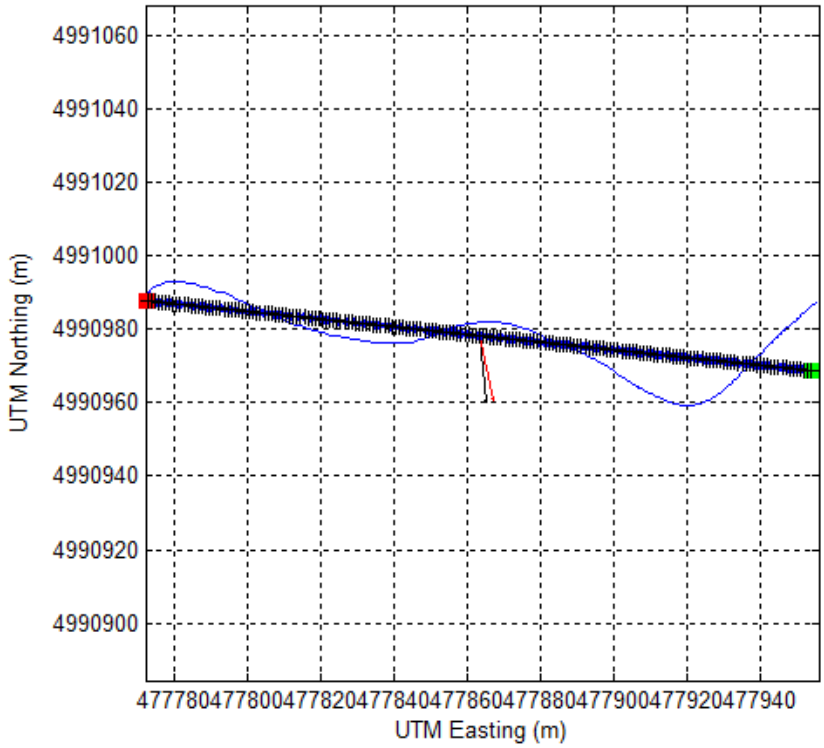

Figure 19: The ship track on cross-section 7 (blue) and the projected one (black) in UTM coordinate. The projected velocity field is valid at certain threshold distance to the plane

First, we analyze the flow dynamics near the confluence (cross-sections 7 to 10). The distribution of velocity magnitude near the confluence is shown in Figure 5. The left branch contributes significant portion of the total discharge. There is a low velocity region near the left branch which deflects the high velocity core toward the midline of the main channel. The mixing interface locates near the centerline of the channel has a significant low velocity core. The right branch possesses a high velocity core. The maximum velocity on this cross-section is in the order of 1.2 m/s.

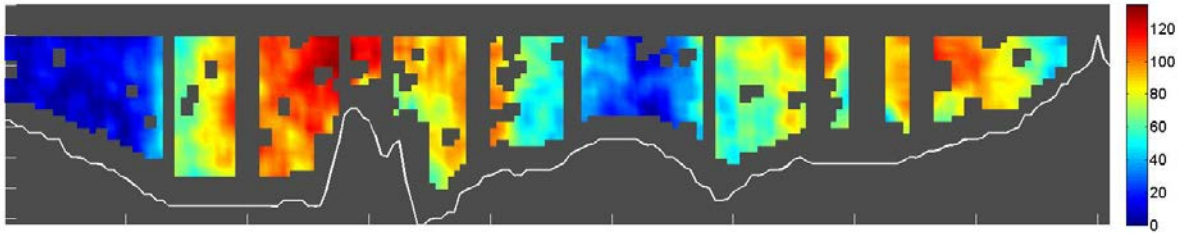

Figure 20: Velocity magnitude distribution on the projected cross-section 7 (Units cm/s)

The dynamics of the flow in the confluence region is highly complex. Figure 6 to Figure **9** show the transitional behavior of the three-dimensional flow in this region. Note that the transverse velocity vectors on the projected cross-section 7 in these figures indicate that the flow is mainly directed from the right branch to the left. However, the velocity vectors in the projected cross-section 8 show that the transverse flow is directed mostly from left branch to right. Moreover, the high velocity's core of the right branch is shifted toward the centerline of the main channel as shown in Figure 7. Small vortices can be visualized near the bottom of the reach.

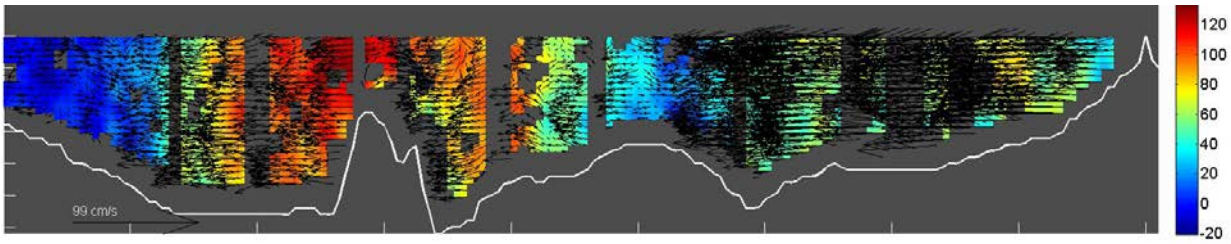

Figure 21: Cross-section 7 (Δx= 20m, Δy = 0.5m, units are in cm/s)

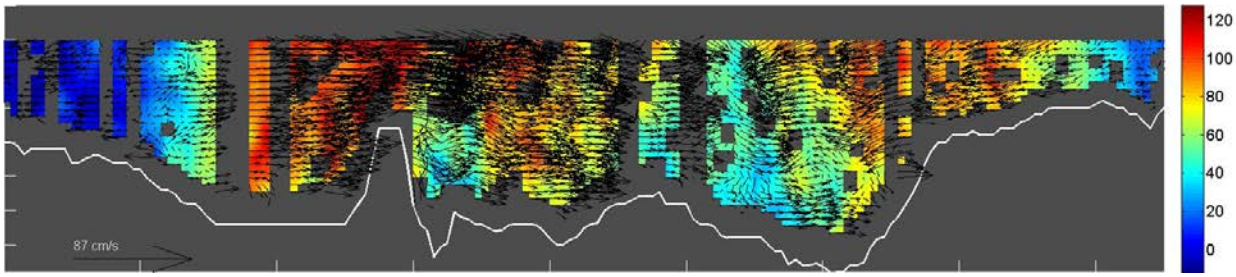

Figure 22: Cross-section 8 (Δx = 20 m Δy =0.5 m, , units are in cm/s)

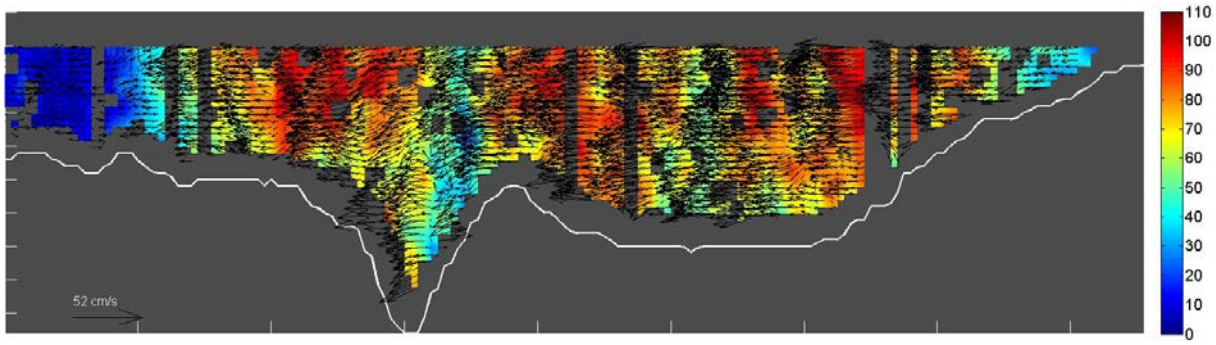

Figure 23: Cross-section 9 (Δx= 20m, Δy = 0.5m, units are in cm/s)

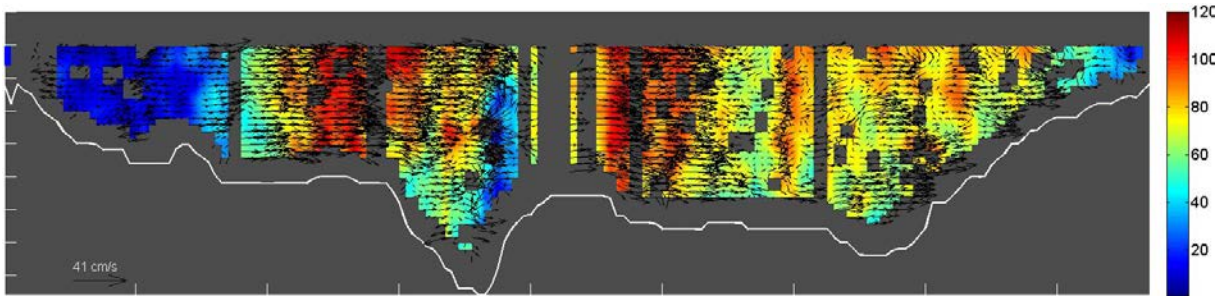

Figure 24: Cross-section 10 (Δx= 20m, Δy = 0.5m, units are in cm/s)

The most interesting phenomenon here is that the large scale structure of the flow exhibits the "flapping" dynamics. As seen in Figure 6 to Figure 9, the transverse flow direction alternate from cross-section to cross-section, indicating that the flow unsteadily meanders along the streamwise direction.

The merging of left and right branches producing a well-mixed region far from the confluence seen in Figure 10 and Figure 11. The high velocity 's core spread out throughout the water column. Visual inspection suggests that velocity fluctuation spatially is large.

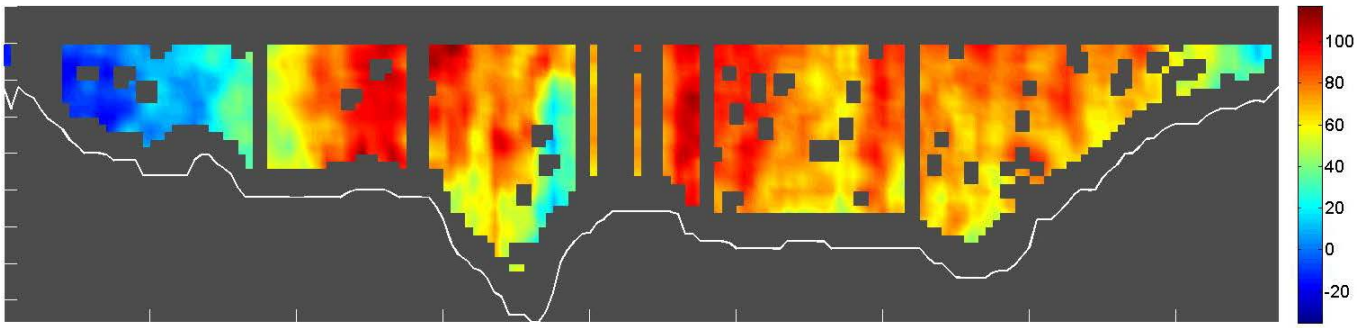

Figure 25: Streamwise component at cross-section 10 (Δx= 20m, Δy = 0.5m, units are in cm/s)

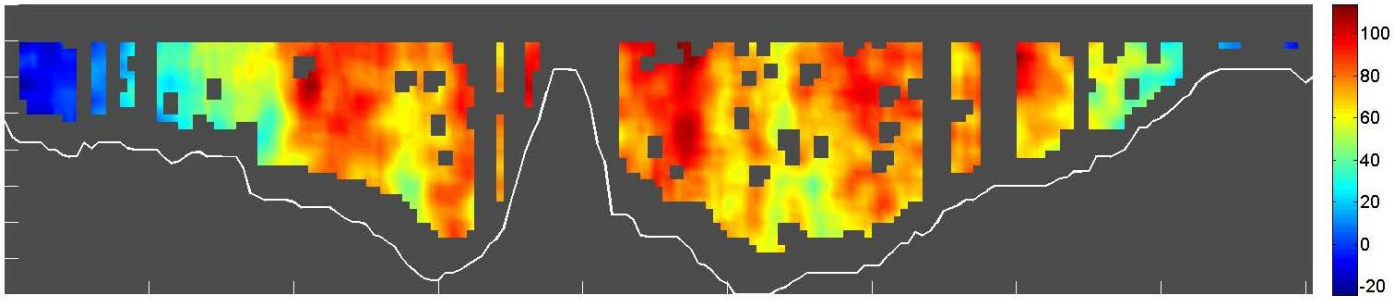

Figure 26: Streamwise component at cross-section 11 (Δx= 20m, Δy = 0.5m, units are in cm/s)

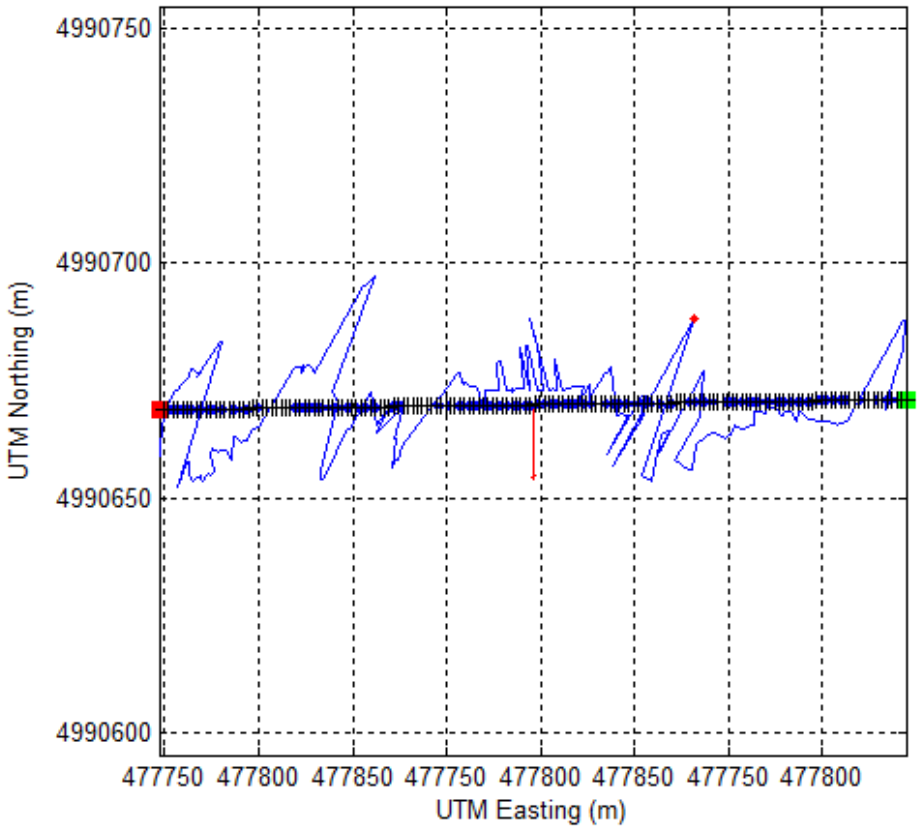

Figure 27: Boat track at cross-section 15 – near the bridge

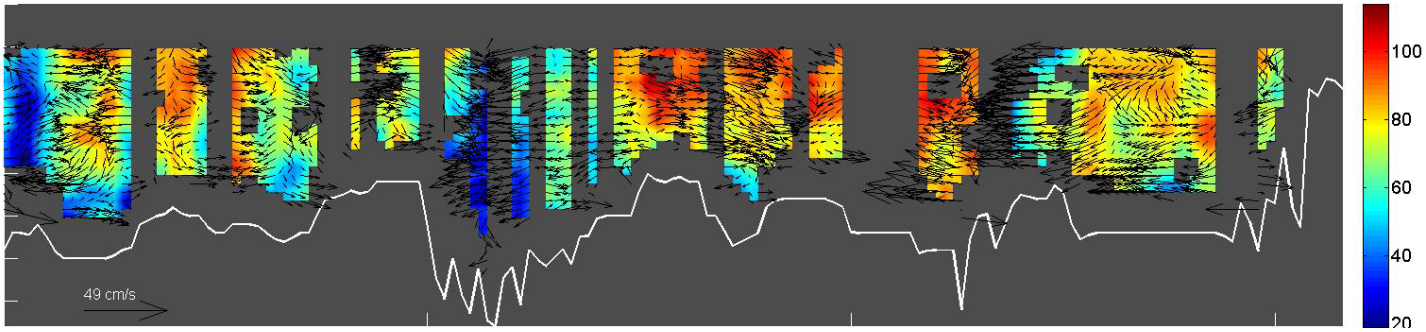

Figure 28: Contour of velocity magnitude and velocity vectors at cross-section 15

As the velocity field in Figure 15 indicates, the interference of the bridge piers to the flow structure is unequivocal.

Hydrodynamic simulations of July 31st, 2014 measurements

Direct comparison of simulated velocity (depth-averaged) with measurements (along the boat-track) are shown in Figure 14. Figure 14 shows the comparison in cross-section 7 using depth-averaged velocity. The flow structure in this section demonstrates clearly the merging of left and right branches. The left branch shows the largest velocity around 1.0 m/s. On the other hand, the right branch shows an extremum of 1.4 m/s. The measured velocity magnitude oscillates largely around the mean, especially on the left branch. This dynamics indicates that unsteadiness play an essential role here during the field measurement.

The simulation results agree wells for both the coarse grid (201) and finer grid (301). In particular, the double-peak structure of the right branch is captured well within the certain degree of agreement.

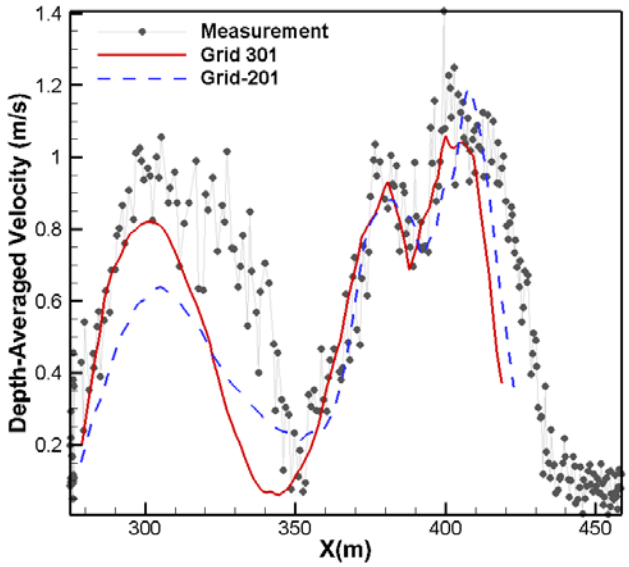

Figure 29: Comparison of velocity magnitude on the Section 7 in local system

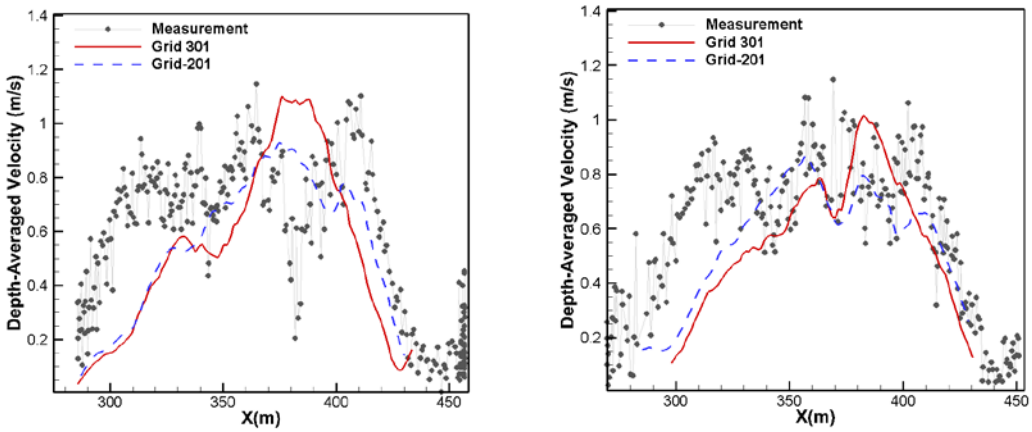

Figure 30: Comparison of velocity magnitude on the Section 10 (left) and 11 (right) in local system

Merging of two branches at lower cross-section 10 and 11 are shown in Figure 15. Here the simulated results underestimate the merging process by providing lower velocity magnitude on the left bank side. This merging process is interfered by the presence of the bridge pier that promotes further mixing and consequently redistributes the momentum of the main channel (see Figure 16 downstream of the bridge).

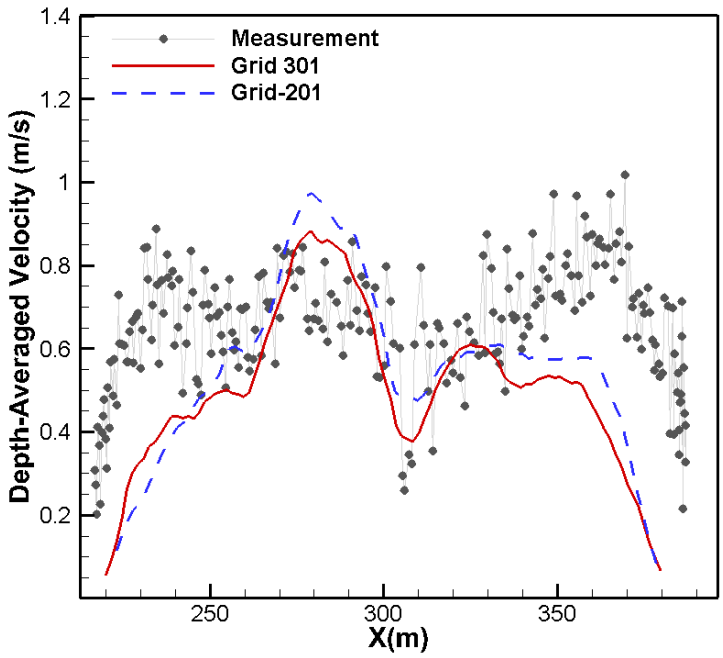

Figure 31: Comparison of velocity magnitude on the Section 16 in local system

Grid sensitivity analysis

In order to analyze the sensitivity of the simulation to the grid we use we carry out the simulation of the 16th May 2014 measurement. The area to comparison is shown in Figure 17 covers the upstream part of

the bridges and the adjacent downstream area. The specific plane to compare is chosen as a constant cross-section at the location Y/H = 220 for accuracy of the comparison.
As observe in Figure 17, the location of the bridge piers and their interaction with the main flow direction are expected to be complex. Note that there are actually three arrays of bridge piers (3 decks) that run parallel to each other. Of noted, the gaps between bridge piers are small and guide the flow through these areas, which renders the flow field to exhibit a fully three-dimensional structure. Comparison of simulated data with different grid resolution illustrates the extent to which these simulation results are sensitive to the input data. Three computational grids shown in Table 3 are used. The results are shown consistently for coarsest grid (gray -201), finer grid (red-301) and very fine grid (401-black). The results shown here are depth-averaged values and presented in the coordinate (transverse –x, streamwise –y, vertical –z) directions.

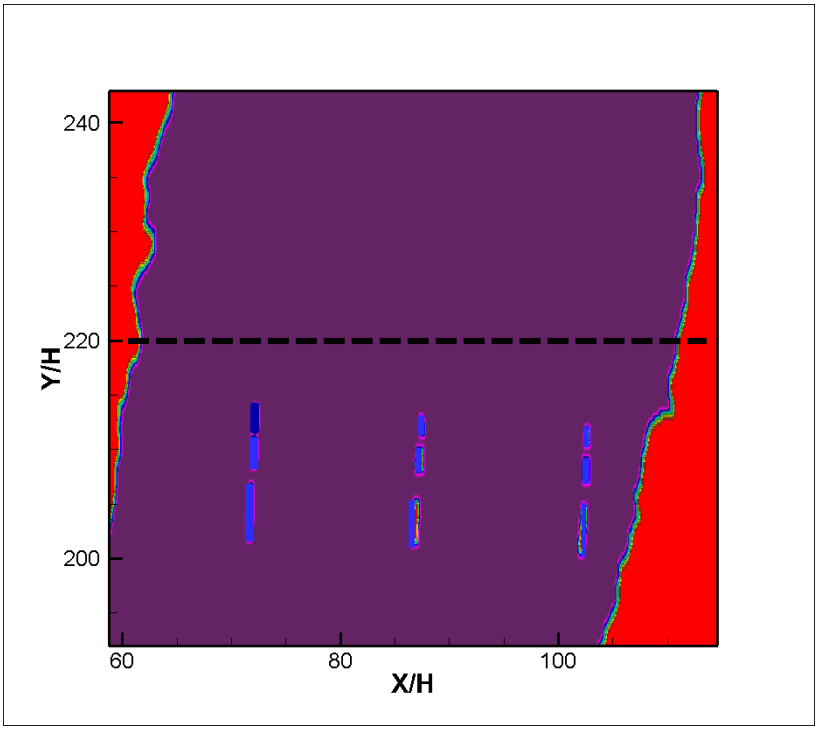

Figure 32: Allocation of bridge piers and the chosen cross-section (dash line) to carry out grid sensitivity analysis

The grid refinement study results for two main components of velocity are shown in Figure 18 and 21 for the streamwise and transverse components, respectively, using depth-averaged quantities. The simulation results show that all of the three grid resolutions obtain similar large scale flow structures. In Figure 18 (streamwise), bridge piers minimally obstruct the main flow component. In Figure 19 (transverse), however, the effect of bridge piers on the transverse flow pattern is clear. Separations can be observed downstream of piers where they interact with other piers. Although the coarsest grid (201) provides primary features of the flow on the mainstream, it does not reflect the dynamics in the vicinity of bridge piers as shown in Figure 19. Note that the finer grid (301-red) provides close similarity to the finest grid (401) at a close examination. This agreement suggests that the finer grid (301) could be used to calculate the hydrodynamic environment at this region.

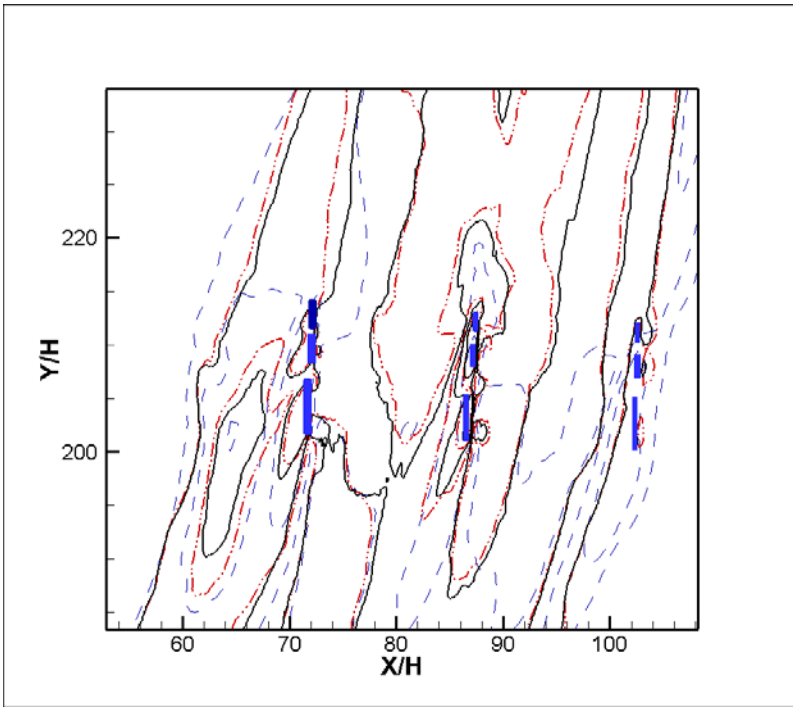

Figure 33: Streamwise component (V) with different grids: coarsest grid (gray -201), finer grid (red-301) and very fine grid (401-black).

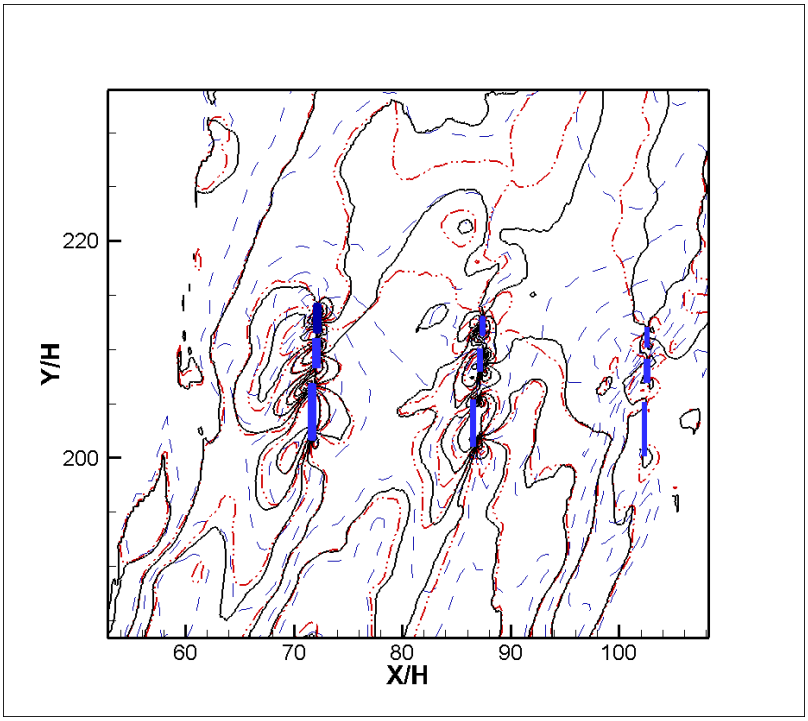

Figure 34: Spanwise component (U) with different grids: Coarsest grid (gray -201), finer grid (red-301), and very fine grid (401-black).

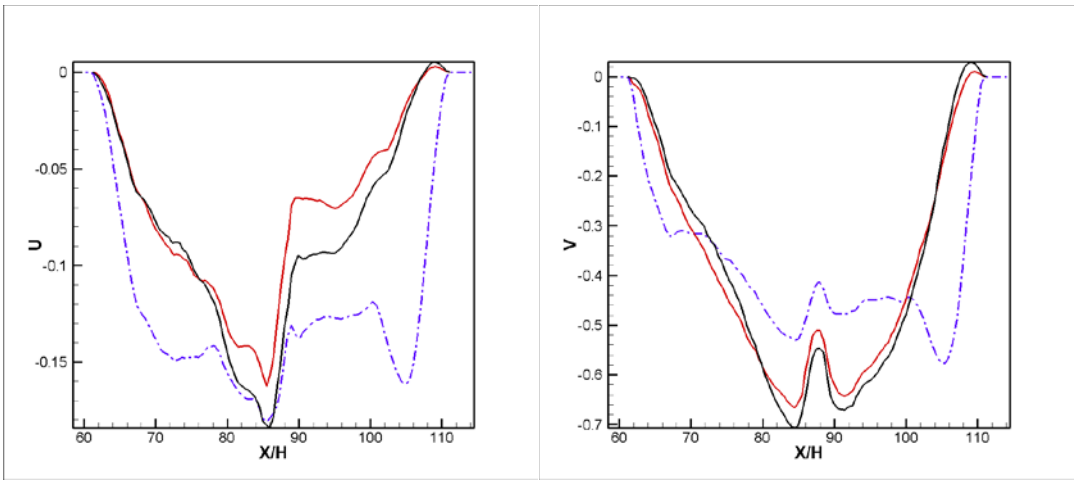

Figure 35: Profile of transverse and streamwise component on the cross-section Y/H = 220 (U): coarsest grid (gray -201), finer grid (red-301) and very fine grid (401-black).

In order to compare the statistical convergence, the turbulent stress components are shown in Figure 21. It can be clearly seen in this figure that the coarse grid (201) does not resolve the fluctuation correctly. The finer grid (301 – red), however, provide sufficient resolution to capture essential dynamics at small scales that converges to the simulation results from the finest grid.

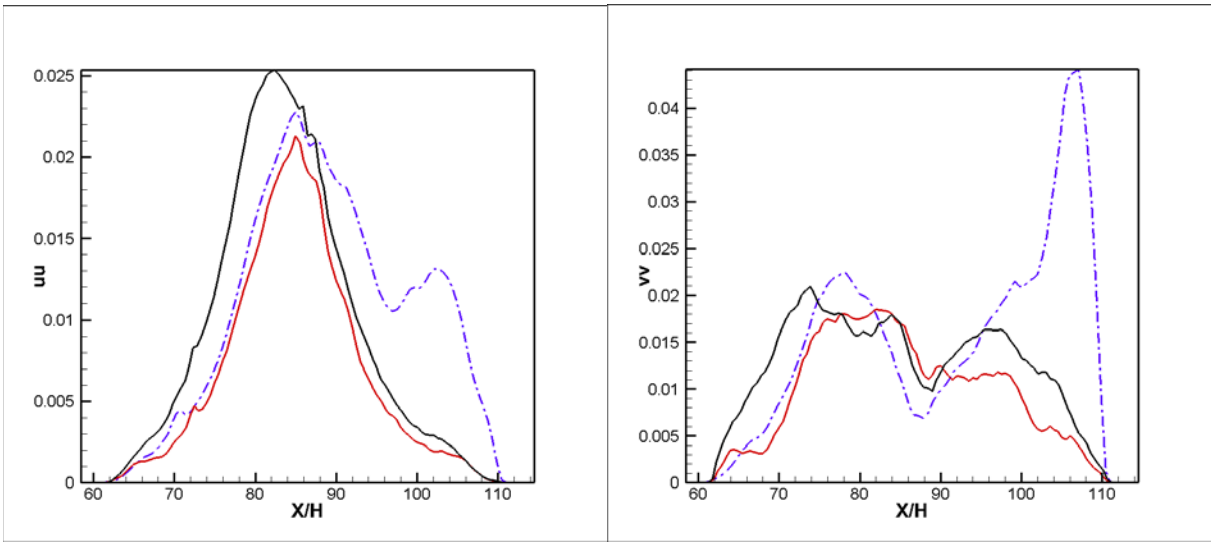

Figure 36: Main turbulent stresses (streamwise and tranverse) coarsest grid (gray -201), finer grid (red-301) and very fine grid (401-black).

Based on our grid sensitivity analysis (the 16th of May 2014) and comparison with the measured data (the 31st of July 2014), we conclude that the fine grid (301) is adequate to provide enough spatial resolution needed for accurate simulations. Hence, the finest grid will be used for the rest of simulations where we solve the fully coupled hydro-morphodynamics equations to simulate flow and sediment transport in the study reach of this project in the Mississippi River.

Conclusions

Here we provide preliminary computational results to validate the numerical model and study the three-dimensional dynamics at the confluence. We also investigated the sensitivity of the numerical solution to the grid resolution and found that the appropriate grid spacing for the problem if the grid 401 with over 100 million computational grid nodes. We found that hydrodynamic conditions during low flow (31 July 2014) and normal flow (16 May 2014) are almost similar. And that the flow mainly concentrates on the right branch with a velocity magnitude in the order of 1 m/s. The flow dynamics during normal discharges is highly unsteady and vortices shedding occur constantly at the confluence immediately downstream of the main island. We also observed that the mixing interface and the shear layer (which originates at the confluence) leads to a large scale meandering. The mixing occurs actively at the downstream of the confluence and further promoted by the presence of bridge piers. Turbulent level and shear stresses at the downstream of the confluence and the vicinity of bridge piers are high suggesting that sediment transport processes in this region could be significantly affected by such phenomena.

References:

Khosronejad, A., Kang, S., and Sotiropoulos, F. (2012), Experimental and computational investigation of local scour around bridge piers. *Advances Water Resources,* 37, 73-85, doi:10.1016/j.advwatres.2011.09.013.

Khosronejad, A., Hill, C., Kang, S., and Sotiropoulos, F., (2013), Experimental and computational investigation of local scour around in-stream restoration structures. *Advances Water Resources,* 57, 191-207, doi:10.1016/j.advwatres.2013.01.008.

Khosronejad, A. and Sotiropoulos, F. (2014), Numerical simulation of sand waves in a turbulent open channel flow, *Journal of Fluid Mechanics*, 753:150-216.

Toso, J. W., Bridge scour investigation, Bridge 9321 and 27801 Intestate Highway 694 over the Mississippi river in Hennepin County, Minnesota Department of Transportation, 1993.